A 2D nonlinear multiring model for blood flow in large elastic arteries

Arthur R. Ghigo, Jose-Maria Fullana, Pierre-Yves Lagrée

Arthur R. Ghigo Jose-Maria Fullana Pierre-Yves Lagrée

Sorbonne Universités, CNRS and UPMC Université Paris 06, UMR 7190, Institut Jean Le Rond ∂'Alembert

A 2D nonlinear multiring model for blood flow in large elastic arteries

Abstract

In this paper, we propose a two-dimensional nonlinear "multiring" model for blood flow in axisymmetric elastic arteries. It is designed to overcome the numerical difficulties of three-dimensional fluid-structure interaction simulations of blood flow without using the over-simplifications necessary to obtain one-dimensional models of blood flow. This multiring model is derived by integrating over concentric rings of fluid the simplified long-wave Navier-Stokes equations coupled to an elastic model of the arterial wall. The resulting system of balance laws provides a unified framework in which both the motion of the fluid and the displacement of the wall are dealt with simultaneously. The mathematical structure of the multiring model allows us to use a finite volume method that guarantees the conservation of mass and the positivity of the numerical solution and can deal with nonlinear flows and large deformations of the arterial wall. We show that the finite volume numerical solution of the multiring model provides at a reasonable computational cost an asymptotically valid description of blood flow velocity profiles and other averaged quantities (wall shear stress, flow rate, ...) in large elastic and quasi-rigid arteries. In particular, we validate the multiring model against well-known solutions such as the Womersley or the Poiseuille solutions as well as against steady boundary layer solutions in quasi-rigid constricted and expanded tubes.

Submitted to the *Journal of Computational Physics*
Contact: arthur.ghigo@dalembert.upmc.fr

Contents

1. Introduction

The numerical simulation of blood flow in large elastic arteries requires the resolution of a complex fluid-structure interaction (FSI) problem. Indeed, the motion of blood is governed by the three-dimensional (3D) Navier-Stokes equations for an incompressible homogeneous Newtonian fluid [48] and the deformation of the arterial wall is described by a nonlinear elastic constitutive law [32]. Several numerical methods have been proposed to solve this nonlinear 3D FSI problem [33, 23, 60, 25, 61, 40]. Due to their modelling complexity and high computational cost, they have only been used to accurately compute blood flow in small regions of interest such as in arterial pathologies or small portions of the systemic network [59, 63, 52]. However, an accurate local analysis is not sufficient to obtain physiological results. Indeed, the observed waveforms in large arteries are the result of the reflection, damping and diffusion throughout the systemic network of the waves emanating from the heart [1, 47]. Realistic waveforms can only be computed by performing a global simulation taking into account a large portion of the arterial network. Unfortunately, such large network 3D FSI simulations are too computationally expensive. Reduced-order models have therefore been proposed to compute physiological waveforms at a lower modeling and computational cost [34, 44, 49, 2, 3]. The aim of this paper is to propose a novel two-dimensional (2D) reduced-order model that accurately computes linear and nonlinear blood flow features in rigid and axisymmetric elastic arteries at a reasonable computational cost with minimal modeling parameters and could prove to be an alternative to 3D FSI simulations in simple arterial configurations.

Reduced-order models for blood flow rely on a simplified system of equations for the motion of blood and a single equation for the deformation of the arterial wall. Assuming that the flow is axisymmetric and noticing that the characteristic length scale in the axial direction is much larger then the one in the radial direction, the Navier-Stokes equations can be simplified in the long-wave asymptotic limit. The resulting system of equations is often referred to as the reduced Navier-Stokes Prandtl (RNS-P) system of equations. It describes the conservation of mass and axial momentum of blood in an axisymmetric artery in which the pressure is hydrostatic (function of x at t only):

$$\begin{cases} \dfrac{1}{r}\dfrac{\partial}{\partial r}\left[r u_r\right] + \dfrac{\partial u_x}{\partial x} = 0 & \text{(1a)} \\ \dfrac{\partial u_x}{\partial t} + u_r\dfrac{\partial u_x}{\partial r} + u_x\dfrac{\partial u_x}{\partial x} = -\dfrac{1}{\rho}\dfrac{\partial p}{\partial x} + \dfrac{\nu}{r}\dfrac{\partial}{\partial r}\left[r\dfrac{\partial u_x}{\partial r}\right] & \text{(1b)} \\ p\left(x,t\right). & \text{(1c)} \end{cases}$$

The axial and radial boundary conditions for system (1) are provided in the next section. Similarly, using simplifying assumptions, different hydrostatic pressure laws $p(x,t)$ can be found linking the motion of the fluid and the displacement of the wall. Depending on the problem addressed, they can describe for example the behavior of flexible viscoelastic rubber tubes in hydraulic systems, the propagation of a water hammer (Allevi's equations) or the deformation of an elastic artery. The later is used in this study and its exact form is given in the following section.

These RNS-P equations (1) are a rich dynamical system able to describe many asymptotic flow regimes in rigid tubes [68, 58, 37]. They were numerically solved in [7, 16] in a rigid axisymmetric tube using a variety of numerical methods. However, similar numerical difficulties to those encountered in 3D FSI problems arise when solving the RNS-P equations (1) in an elastic tube.

One-dimensional (1D) models were therefore introduced as simple and efficient methods to obtain averaged quantities in elastic arteries [22, 38, 28, 43, 65]. They are obtained by averaging over the cross-sectional area of the artery the mass (1a) and momentum (1b) equations. Unfortunately, they depend on coefficients which themselves depend on the shape of the velocity profile, lost in the averaging process. These coefficients are therefore estimated *a priori*, which often results in unrealistic viscous dissipation and pressure losses.

One-and-a-half-dimensional (3/2D) models were then proposed as intermediates between 1D models and the complete resolution of the RNS-P equations (1). In [14, 13], the authors used an asymptotic analysis of the RNS-P equations (1) and homogenization theory to propose a 3/2D model for blood flow in an elastic artery. This model allows to compute, without any *a priori* coefficient estimation, the zero-th and first order components of the wall displacement and the axial and radial velocities. In [9], an approximate velocity profile function was obtained depending on the instantaneous pressure gradient and the thickness of the boundary layer. This function was then used in a 1D model to compute the velocity profile-dependent coefficients. In [36], a Von Kármán-Polhlausen integral method closed using the Womersley velocity profiles was studied. This integral method accurately computes linear solutions such as the Womersley solution [68] but is limited by the chosen linear closure relation. More recently, in [27], the authors proposed an analytic model for blood flow in an elastic artery based on a generalized Darcy's model and the linear Womersley theory. Despite their added modeling precision, 3/2D models still only provide approximate solutions of the RNS-P equations (1).

Several authors have therefore proposed numerical methods to directly solve the RNS-P equations (1) in elastic arteries. A noteworthy attempt was presented in [39] but the problem was simplified by introducing an explicit dependence with experimental data. In [36], the author derived a boundary layer method which gives good results in the linear regime but behaves poorly in the nonlinear regime. To our knowledge, the most advanced numerical method was proposed in [15]. There, a semi-implicit efficient numerical method was introduced based on an Eulerian-Lagragian method to treat the advection term and a nested Newton algorithm to iteratively compute the pressure matching the desired wall displacement. The main drawback of this approach is that it can not deal with arbitrary large wall deformation and requires that the flow stays mildly nonlinear.

In this work, we propose a novel 2D model to solve without any approximations the RNS-P equations (1) in elastic arteries for arbitrary large arterial wall deformations. By decomposing the fluid domain in concentric rings, we derive what we refer to as the "multiring model with mass exchange". This model is inspired from the multilayer model with mass exchange presented in [6] in the context of shallow water equations. This multiring system of balance laws provides a unified framework in which both the motion of the fluid and the displacement of the wall are dealt with simultaneously. Its mathematical structure allows us to use a *finite volume* numerical method that guarantees the conservation of mass and the positivity of the numerical solution and can deal with nonlinear flows and large deformations of the arterial wall. We will show that the multiring model can compute all relevant flow features in elastic arteries.

In the first section, we present the derivation of the multiring model. Next, we discuss its mathematical properties and details of the numerical method. In the last sections, we propose a series a examples where we compare the solution of the multiring model to reference solutions in elastic and quasi-rigid arteries.

2. A multiring discretization of the RNS-P equations

We describe a multiring model with mass exchange for blood flow based on the axisymmetric RNS-P equations (1) coupled to an elastic wall model. As stated in the introduction, this multiring model is the analog of the multilayer model with mass exchange for shallow water flows [6].

2.1. Radial decomposition of the fluid domain

In the framework of the axisymmetric RNS-P equations (1), the arteries are modeled as axisymmetric cylinders of radius R, cross-sectional area $A = \pi R^2$ and length L. Therefore, we can divide the fluid region delimited by the arterial wall into N_r concentric axisymmetric rings of width h_α, with $\alpha = 1, ..., N_r$. This decomposition of the fluid domain is illustrated in figure 1. To simplify the notations, we refer to the fluid ring of width h_α as the ring α. Each ring α is delimited by an upper and lower interface, respectively defined by the radii $R_{\alpha+\frac{1}{2}}$ and $R_{\alpha-\frac{1}{2}}$, with:

$$h_\alpha = R_{\alpha+\frac{1}{2}} - R_{\alpha-\frac{1}{2}}. \tag{2}$$

The interface position $R_{\alpha+\frac{1}{2}}$ and the radius of the artery R can now respectively be written as:

$$R_{\alpha+\frac{1}{2}} = \sum_{j=1}^{\alpha} h_j, \quad R = \sum_{j=1}^{N_r} h_j. \tag{3}$$

We also define the cross-sectional area of the ring α, noted A_α, the average flow rate in the ring α, noted Q_α, and the mean velocity in the ring α, noted u_α:

$$\begin{cases} A_\alpha = \displaystyle\int_0^{2\pi} \int_{R_{\alpha-\frac{1}{2}}}^{R_{\alpha+\frac{1}{2}}} r dr d\theta \\ Q_\alpha = \displaystyle\int_0^{2\pi} \int_{R_{\alpha-\frac{1}{2}}}^{R_{\alpha+\frac{1}{2}}} u_x r dr d\theta \\ u_\alpha = \dfrac{Q_\alpha}{A_\alpha}. \end{cases} \tag{4}$$

Finally, we note $l_{r,\alpha}$ the proportion of the total radius R occupied by the ring α:

$$h_\alpha = l_{r,\alpha} R \quad \text{with} \quad \sum_{\alpha=1}^{N_r} l_{r,\alpha} = 1, \tag{5}$$

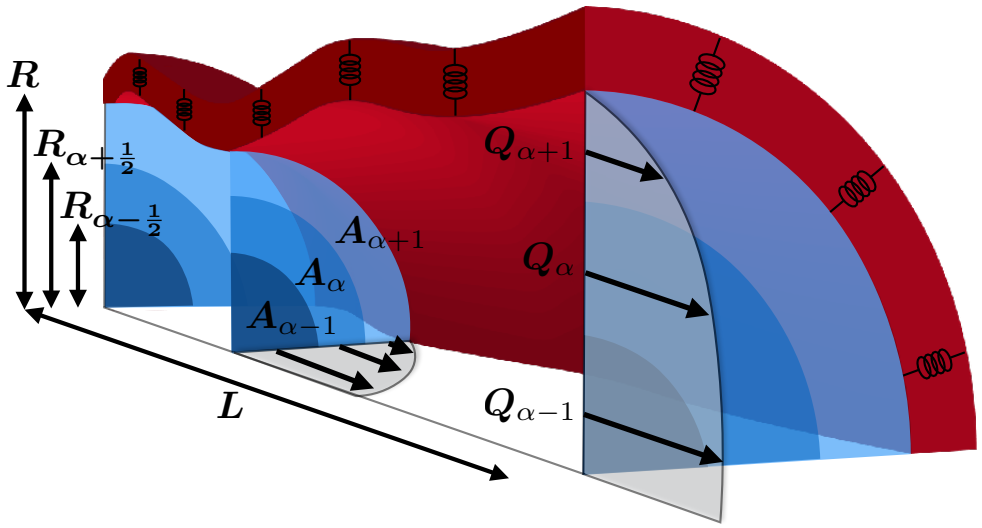

Figure 1: *Representation of the decomposition in several concentric rings of the fluid domain contained in an axisymmetric cylindrical artery. For clarity, only one-fourth of the artery of length L is represented. The springs in the arterial wall represent its elastic behavior. The variable Q_α is the flow rate in the ring α and A_α is the area delimited by the radii $R_{\alpha-\frac{1}{2}}$ and $R_{\alpha+\frac{1}{2}}$*

and l_α the proportion of the total cross-sectional area A occupied by the ring α:

$$A_\alpha = l_\alpha A \quad \text{with} \quad l_\alpha = \left(\sum_{j=1}^{\alpha} l_{r,j}\right)^2 - \left(\sum_{j=1}^{\alpha-1} l_{r,j}\right)^2 . \tag{6}$$

Without loss of generality, we prescribe the radial decomposition of the artery in concentric rings and set the proportion $l_{r,\alpha}$ in each ring α. This proportion is therefore a given constant number which can differ from one ring to another:

$$\forall t \geq 0, \quad \forall x \in [0, L], \quad l_{r,\alpha} = \text{cst} \quad \text{with} \quad \alpha = 1, ..., N_r. \tag{7}$$

As a consequence, we have:

$$\forall t \geq 0, \quad \forall x \in [0, L], \quad l_{\alpha} = \text{cst} \quad \text{with} \quad \alpha = 1, ..., N_r. \tag{8}$$

Assumption (7) indicates that the interfaces $R_{\alpha-\frac{1}{2}}$ and $R_{\alpha+\frac{1}{2}}$ of the ring α are not impermeable interfaces but rather interfaces of a radial mesh, and therefore mass exchanges exist between neighboring rings. This radial mesh automatically adapts itself to the movement of the arterial wall and can sustain arbitrary large wall deformation as long as $R > 0$.

We will use this decomposition of the fluid domain in concentric rings to introduce a *finite volume* discretization of the axisymmetric RNS-P equations (1) in the radial direction.

2.2. System of equations for one layer

Inspired by *finite volume* methods, we integrate the axisymmetric RNS-P equations (1) over the cross-sectional area the ring α:

$$\int_0^{2\pi} \int_{R_{\alpha-\frac{1}{2}}}^{R_{\alpha+\frac{1}{2}}} \left\{ \begin{array}{l} \dfrac{1}{r}\dfrac{\partial}{\partial r}\left[r u_r\right] + \dfrac{\partial u_x}{\partial x} = 0 \\ \dfrac{\partial u_x}{\partial t} + u_r \dfrac{\partial u_x}{\partial r} + u_x \dfrac{\partial u_x}{\partial x} = -\dfrac{1}{\rho}\dfrac{\partial p}{\partial x} + \dfrac{\nu}{r}\dfrac{\partial}{\partial r}\left[r \dfrac{\partial u_x}{\partial r}\right] \end{array} \right\} r \, \mathrm{d}r \, \mathrm{d}\theta. \tag{9}$$

Using the Leibniz integration rule, we obtain an integral form of the axisymmetric RNS-P mass and momentum equations (resp. eq. (1a) and (1b)) in the ring α:

$$\begin{cases} \dfrac{\partial A_\alpha}{\partial t} + \dfrac{\partial Q_\alpha}{\partial x} = G_{\alpha+\frac{1}{2}} - G_{\alpha-\frac{1}{2}} & \text{(10a)} \\ \dfrac{\partial Q_\alpha}{\partial t} + \dfrac{\partial}{\partial x}\left(\psi_\alpha \dfrac{Q_\alpha^2}{A_\alpha}\right) + \dfrac{A_\alpha}{\rho}\dfrac{\partial p}{\partial x} = S_{M,\alpha} + S_{\nu,\alpha}. & \text{(10b)} \end{cases}$$

The term $G_{\alpha+\frac{1}{2}}$ represents the radial mass exchanges at the interface $R_{\alpha+\frac{1}{2}}$ and is defined as:

$$G_{\alpha+\frac{1}{2}} = \frac{\partial}{\partial t}\left[\pi R_{\alpha+\frac{1}{2}}^2\right] + u_{x,\alpha+\frac{1}{2}}\frac{\partial}{\partial x}\left[\pi R_{\alpha+\frac{1}{2}}^2\right] - 2\pi R_{\alpha+\frac{1}{2}} u_{r,\alpha+\frac{1}{2}}. \tag{11}$$

The source term $S_{M,\alpha}$ characterizes the momentum associated to the radial mass exchanges in the ring α and writes:

$$S_{M,\alpha} = u_{x,\alpha+\frac{1}{2}} G_{\alpha+\frac{1}{2}} - u_{x,\alpha-\frac{1}{2}} G_{\alpha-\frac{1}{2}}, \tag{12}$$

where $u_{x,\alpha+\frac{1}{2}} = u_x\left(x, R_{\alpha+\frac{1}{2}}, t\right)$ is the axial velocity in $R_{\alpha+\frac{1}{2}}$. The source term $S_{\nu,\alpha}$ describes the viscous dissipation in the ring α and writes:

$$S_{\nu,\alpha} = 2\pi\nu\left(\left[r\frac{\partial u_x}{\partial r}\right]_{R_{\alpha+\frac{1}{2}}} - \left[r\frac{\partial u_x}{\partial r}\right]_{R_{\alpha-\frac{1}{2}}}\right). \tag{13}$$

Finally, the nonlinear advection correction coefficient ψ_α writes:

$$\psi_\alpha = \frac{A_\alpha}{Q_\alpha^2}\int_{R_{\alpha-\frac{1}{2}}}^{R_{\alpha+\frac{1}{2}}} 2\pi r\, u_x^2 dr. \tag{14}$$

It is important to note that up to this point, the integration process is exact and no approximation has been made in this *finite volume* radial discretization of the axisymmetric RNS-P equations (1). We will now derive the system of equations governing the motion of blood in the entire artery.

2.3. System of equations for the artery

To obtain the system of equations governing blood flow in the entire artery, we must combine the N_r system of equations (10) describing the conservation of mass and axial momentum in each ring α. The unknowns of the global system are therefore the cross-sectional area A_α and the flow rate Q_α of each ring α.

However, an important consequence of assumption (7) is that the local cross-sectional area A_α can be deduced from the cross-sectional area A using the prescribed proportion l_α. The unknowns of the system are then reduced to the cross-sectional area A and the flow rate Q_α of each ring α. Similarly, by adding the N_r mass conservation equations (10a), we obtain a single mass conservation equation depending on the cross-sectional area A and the flow rate Q_α of each ring α:

$$\frac{\partial A}{\partial t} + \frac{\partial}{\partial x}\left[\sum_{j=1}^{N_r} Q_j\right] = G_{N_r+\frac{1}{2}} - G_{\frac{1}{2}}. \tag{15}$$

Performing the same operation but adding only up to the ring α, we obtain the following expression for the mass exchange term $G_{\alpha+\frac{1}{2}}$:

$$G_{\alpha+\frac{1}{2}} - \left[G_{N_r+\frac{1}{2}}\sum_{j=1}^{\alpha} l_j + G_{\frac{1}{2}}\sum_{j=\alpha+1}^{N_r} l_j\right] = \sum_{j=1}^{\alpha}\left[\frac{\partial Q_j}{\partial x} - l_j\sum_{p=1}^{N_r}\left[\frac{\partial Q_p}{\partial x}\right]\right]. \tag{16}$$

Finally, by combining the previous remarks, we obtain a simplified global system of equations describing the conservation of mass in the artery and the conservation of axial momentum in each ring α. We refer to

this system as the multiring system of equations, which depends on the variables $[A, Q_1, ..., Q_\alpha, ..., Q_{N_r}, p]$ and writes:

$$\begin{cases} \dfrac{\partial A}{\partial t} + \dfrac{\partial}{\partial x}\left[\displaystyle\sum_{j=1}^{N_r} Q_j\right] = G_{N_r+\frac{1}{2}} - G_{\frac{1}{2}} & \text{(17a)} \\ \dfrac{\partial Q_\alpha}{\partial t} + \dfrac{\partial}{\partial x}\left(\psi_\alpha \dfrac{Q_\alpha^2}{l_\alpha A}\right) + l_\alpha \dfrac{A}{\rho}\dfrac{\partial p}{\partial x} = S_{M,\alpha} + S_{\nu,\alpha}, \quad \text{for} \quad \alpha = 1, ..., N_r. & \text{(17b)} \end{cases}$$

We will now provide a closure relation linking the pressure p with the cross-sectional area A and describing the elastic behavior of the arterial wall.

2.4. Pressure law

We assume that the artery is an incompressible, isotropic and homogeneous thin-walled elastic cylinder and that each section of the wall moves independently of the others. Under these hypotheses, the transmural hydrostatic pressure can be expressed as (see [55, 28, 43, 65] for details):

$$p(x,t) - p_0 = K(x)\left(\sqrt{A(x,t)} - \sqrt{A_0(x)}\right). \tag{18}$$

The variables A_0 and K respectively represent the cross-sectional area at rest (when there is no flow) and the arterial wall rigidity. Both can vary with the axial position x. The variable p_0 is the pressure applied on the exterior of the arterial wall and is assumed constant in the following.

2.5. Radial boundary conditions

To complete the description of the system of equations (17), we provide boundary conditions at center of the artery, in $r = R_{\frac{1}{2}} = 0$, and at the arterial wall, in $r = R_{N_r+\frac{1}{2}} = R$.

In the center of the artery, in $r = R_{\frac{1}{2}}$, the velocity must verify the following axisymmetric boundary conditions:

$$\frac{\partial u_x}{\partial r}|_{R_{\frac{1}{2}}} = 0 \quad \text{and} \quad u_r|_{R_{\frac{1}{2}}} = 0. \tag{19}$$

At the arterial wall, in $r = R_{N_r+\frac{1}{2}}$, the following classical kinematic boundary condition is verified stating that the arterial wall is a material interface:

$$2\pi R_{N_r+\frac{1}{2}} u_{r,N_r+\frac{1}{2}} - \frac{\partial}{\partial t}\left[\pi R_{N_r+\frac{1}{2}}^2\right] - u_{x,N_r+\frac{1}{2}}\frac{\partial}{\partial x}\left[\pi R_{N_r+\frac{1}{2}}^2\right] = 0. \tag{20}$$

Since we have assumed that each section of the wall moves independently of the others, which is a consequence of the fact that the axial stress at the wall is negligible compared to the radial stress, the following no-slip boundary conditions is also verified at the arterial wall, in $r = R_{N_r+\frac{1}{2}}$:

$$u_{x,N_r+\frac{1}{2}} = 0. \tag{21}$$

As a result, the expressions of mass exchange terms $G_{\frac{1}{2}}$ and $G_{N_r+\frac{1}{2}}$ can be simplified using the boundary conditions (19) and (20):

$$G_{\frac{1}{2}} = 0, \qquad G_{N_r+\frac{1}{2}} = 0. \tag{22}$$

Equations (22) indicate that there is no mass exchange at the arterial wall due to its impermeability and that there is no mass exchange in the center of the artery due to the axisymmetry of the flow.

2.6. Multiring system of equations

Injecting the pressure law (18) and the boundary conditions (22) in the multiring system of equations (17), we obtain the final closed-form of the multiring system of equations describing the conservation of mass and axial momentum in an elastic impermeable axisymmetric artery:

$$\frac{\partial A}{\partial t} + \frac{\partial F_A}{\partial x} = 0 \tag{23a}$$

$$\frac{\partial Q_\alpha}{\partial t} + \frac{\partial F_{Q_\alpha}}{\partial x} = S_{M,\alpha} + S_{\nu,\alpha} + l_\alpha S_T, \quad \text{for} \quad \alpha = 1, ..., N_r, \tag{23b}$$

where:

$$\begin{cases} F_A = \sum_{j=1}^{N_r} Q_j & \text{(24a)} \\ F_{Q_\alpha} = \psi_\alpha \frac{Q_\alpha^2}{l_\alpha A} + l_\alpha \frac{K}{3\rho} A^{\frac{3}{2}}, & \text{(24b)} \end{cases}$$

and:

$$S_T = \frac{A}{\rho}\left(\frac{\partial}{\partial x}\left(K\sqrt{A_0}\right) - \frac{2}{3}\sqrt{A}\frac{\partial K}{\partial x}\right). \tag{25}$$

The source term S_T is the geometrical and mechanical source term and is non-zero when the cross-sectional area at rest A_0 or the arterial wall rigidity K vary with the axial position x. The mass exchange source term $S_{M,\alpha}$ is defined by expression (12) and the viscous source term by expression (13). The expression (16) for the mass exchange term $G_{\alpha+\frac{1}{2}}$ in each ring α can be simplified using the boundary conditions (22):

$$G_{\alpha+\frac{1}{2}} = \sum_{j=1}^{\alpha}\left[\frac{\partial Q_j}{\partial x} - l_j \sum_{p=1}^{N_r}\left[\frac{\partial Q_p}{\partial x}\right]\right] \tag{26}$$

In the remainder of the study, we assume that the advection correction coefficient $\psi_\alpha = 1$ in each ring α. Doing so, we suppose that the velocity profile is a piece-wise constant function of the variable r. This classical *finite volume* hypothesis is the only one used in the derivation of the multiring system of equations and is reasonable if we use a sufficiently large number of rings N_r.

2.7. Radial velocity u_r

We compute the radial velocity u_r using the incompressibility condition (1a). By integrating equation (1a) over the cross-sectional area of the ring α, we obtain:

$$[ru_r]_{R_{\alpha+\frac{1}{2}}} = [ru_r]_{R_{\alpha-\frac{1}{2}}} - \int_{R_{\alpha-\frac{1}{2}}}^{R_{\alpha+\frac{1}{2}}} r\frac{\partial u_x}{\partial x}\mathrm{d}x. \tag{27}$$

The axisymmetric boundary condition (19) imposes that:

$$u_{r,\frac{1}{2}} = 0. \tag{28}$$

We then iteratively compute the radial velocity $u_{r,\alpha+\frac{1}{2}}$ in each ring α using equation (27), and then an approximation of $u_{r,\alpha}$ as:

$$u_{r,\alpha} = \frac{u_{r,\alpha-\frac{1}{2}} + u_{r,\alpha+\frac{1}{2}}}{2}. \tag{29}$$

2.8. Link to the one-dimensional blood flow equations

The multiring system of equations (23) is a generalization of the classical 1D system of equations for blood flow. Indeed, by adding the momentum conservation equations (23b) of all the rings α, we obtain the following global momentum conservation equation:

$$\frac{\partial Q}{\partial t} + \frac{\partial}{\partial x}\left[\sum_{\alpha=1}^{N_r} F_{Q_\alpha}\right] = \sum_{\alpha=1}^{N_r}\left[S_{M,\alpha} + S_{\nu,\alpha} + l_\alpha S_T\right], \tag{30}$$

where:

$$Q = \sum_{\alpha=1}^{N_r} Q_\alpha. \tag{31}$$

Using the boundary conditions (22), the equation (30) simplifies to:

$$\frac{\partial Q}{\partial t} + \frac{\partial}{\partial x}\left[\left[\sum_{\alpha=1}^{N_r}\frac{Q_\alpha^2}{l_\alpha A}\right] + \frac{K}{3\rho}A^{\frac{3}{2}}\right] = 2\pi\nu\left[r\frac{\partial u_x}{\partial r}\right]_{R_{N_r+\frac{1}{2}}} + S_T. \tag{32}$$

Combining the mass conservation equation (23a) with the equation (32), we obtain the following 1D system of equations for blood flow, describing the conservation of mass and axial momentum in an elastic artery:

$$\begin{cases} \dfrac{\partial A}{\partial t} + \dfrac{\partial Q}{\partial x} = 0 & \text{(33a)} \\ \dfrac{\partial Q}{\partial t} + \dfrac{\partial}{\partial x}\left[\left[\displaystyle\sum_{\alpha=1}^{N_r} \frac{Q_\alpha^2}{l_\alpha A}\right] + \frac{K}{3\rho} A^{\frac{3}{2}}\right] = 2\pi\nu \left[r\frac{\partial u_x}{\partial r}\right]_{R_{N_r+\frac{1}{2}}} + S_T. & \text{(33b)} \end{cases}$$

The remaining unknowns are the nonlinear advection term $\sum_{\alpha=1}^{N_r} \frac{Q_\alpha^2}{l_\alpha A}$ and the viscous term $2\pi\nu \left[r\frac{\partial u_x}{\partial r}\right]_{R_{N_r+\frac{1}{2}}}$. They depend of the shape of the axial velocity profile $u_x(x,r,t)$. As it can not be computed by 1D models, it is classical to close system (33) by prescribing an *a priori* shape of the velocity profile. As an example, if we assume that the velocity profile is a Poiseuille profile, we have as in [51]:

$$\sum_{\alpha=1}^{N_r} \frac{Q_\alpha^2}{l_\alpha A} \approx \frac{4}{3}\frac{Q^2}{A} \quad \text{and} \quad 2\pi\nu \left[r\frac{\partial u_x}{\partial r}\right]_{R_{N_r+\frac{1}{2}}} = -8\pi\nu\frac{Q}{A}. \tag{34}$$

Unfortunately, in the vast majority of flow configurations, the *a priori* shape of the velocity profile is an unknown function of time and position and the estimation of the coefficients $\sum_{\alpha=1}^{N_r} \frac{Q_\alpha^2}{l_\alpha A}$ and $2\pi\nu \left[r\frac{\partial u_x}{\partial r}\right]_{R_{N_r+\frac{1}{2}}}$ will therefore be erroneous. We propose the multiring model (23) to overcome those difficulties. Indeed, by integrating over concentric rings of fluid the axisymmetric RNS-P equations (1) coupled to the elastic pressure law (18), we have derived a quasi-analytic radial discretization of the RNS-P equations (1). The resulting multiring system of equations can compute the velocity profile and therefore does not depend on unknown coefficients like all 1D models. It is a system of balance laws, where the left hand side is written as a system of conservation laws and the right hand side contains the mass, viscous and geometrical and mechanical source terms. This mathematical structure guarantees the conservation of mass and axial momentum and is conductive to a *finite volume* axial discretization.

Next, we study the mathematical properties of this system of balance laws.

3. Mathematical properties

We study the mathematical properties of both the single layer system of equations (10) and the multiring system of equations (23).

3.1. Single layer system of equations

We consider here the homogeneous form of the single layer system of equations (10):

$$\begin{cases} \dfrac{\partial A_\alpha}{\partial t} + \dfrac{\partial Q_\alpha}{\partial x} = 0 & \text{(35a)} \\ \dfrac{\partial Q_\alpha}{\partial t} + \dfrac{\partial F_{Q_\alpha}}{\partial x} = 0. & \text{(35b)} \end{cases}$$

This conservative system has been thoroughly studied by many authors and we only briefly recall its properties. Additional details can be found in [28, 65].

The Jacobian matrix of system (35) has two real eigenvalues $\lambda_{1,\alpha}$ and $\lambda_{2,\alpha}$, respectively associated to two right eigenvectors $\boldsymbol{R_{1,\alpha}}$ and $\boldsymbol{R_{2,\alpha}}$:

$$\lambda_{1,\alpha} = \frac{Q_\alpha}{A_\alpha} - c, \quad \lambda_{2,\alpha} = \frac{Q_\alpha}{A_\alpha} + c, \qquad \boldsymbol{R_{1,\alpha}} = \begin{bmatrix} 1 \\ \lambda_{1,\alpha} \end{bmatrix}, \quad \boldsymbol{R_{2,\alpha}} = \begin{bmatrix} 1 \\ \lambda_{2,\alpha} \end{bmatrix}, \tag{36}$$

where c is the Moens-Korteweg celerity [41, 35] and corresponds to the celerity of a pulse wave:

$$c = \sqrt{\frac{K}{2\rho}\sqrt{A}}. \tag{37}$$

The hyperbolicity of system (35) is characterized by the Shapiro number $S_{h,\alpha}$, introduced by Shapiro in [54]:

$$S_{h,\alpha} = \frac{u_\alpha}{c}. \tag{38}$$

The Shapiro number $S_{h,\alpha}$ is the analog of the Froude number F_r for the shallow water equations or of the Mach number M_a for compressible flows. Depending on the value of $S_{h,\alpha}$, we distinguish two flow regimes in the ring α: if $S_{h,\alpha} < 1$, the flow is subcritical and if $S_{h,\alpha} > 1$ the flow is supercritical. In both cases, system (35) is strictly hyperbolic as $\lambda_{1,\alpha} \neq \lambda_{2,\alpha}$ and the right eigenvectors $\boldsymbol{R_{1,\alpha}}$ and $\boldsymbol{R_{2,\alpha}}$ are linearly independent. In physiological conditions, blood flow is almost always subcritical [57], and therefore we will only consider the case $S_{h,\alpha} < 1$. The Riemann invariant vector $\boldsymbol{W_\alpha}$ associated with the system (35) is:

$$\boldsymbol{W_\alpha} = \begin{bmatrix} W_{1,\alpha} \\ W_{2,\alpha} \end{bmatrix} = \begin{bmatrix} \frac{Q_\alpha}{A_\alpha} - 4c \\ \\ \frac{Q_\alpha}{A_\alpha} + 4c \end{bmatrix}. \tag{39}$$

The vector $\boldsymbol{W_\alpha}$ is linked to the conservative variables through the following relations:

$$\begin{cases} A_\alpha = \left(\dfrac{2\rho}{K}\right)^2 \left(\dfrac{W_{2,\alpha} - W_{1,\alpha}}{8}\right)^4 \\ Q_\alpha = A_\alpha \dfrac{W_{1,\alpha} + W_{2,\alpha}}{2}. \end{cases} \tag{40}$$

The relations (40) will be useful in the following to define the boundary conditions at the inlet and outlet of the computational domain.

3.2. Two layers system of equations

We now focus on the more complicated inviscid two layers system of equations:

$$\begin{cases} \dfrac{\partial A}{\partial t} + \dfrac{\partial F_A}{\partial x} = 0 & \text{(41a)} \\ \dfrac{\partial Q_1}{\partial t} + \dfrac{\partial F_{Q_1}}{\partial x} = S_{M,1} & \text{(41b)} \\ \dfrac{\partial Q_2}{\partial t} + \dfrac{\partial F_{Q_2}}{\partial x} = S_{M,2}. & \text{(41c)} \end{cases}$$

To simplify the analysis, we suppose that the geometrical and mechanical properties of the artery do not vary ($S_T = 0$). This system can be written in the following quasi-linear form:

$$\boldsymbol{M}(\boldsymbol{X}) \frac{\partial \boldsymbol{X}}{\partial t} + \boldsymbol{H}(\boldsymbol{X}) \frac{\partial \boldsymbol{X}}{\partial x} = 0. \tag{42}$$

The vector $\boldsymbol{X}$ and the matrices $\boldsymbol{M}$ and $\boldsymbol{H}$ are respectively defined as:

$$\boldsymbol{X} = \begin{bmatrix} A \\ \bar{Q}_1 \\ \bar{Q}_2 \end{bmatrix}, \ \boldsymbol{M}(\boldsymbol{X}) = \begin{bmatrix} 1 & 0 & 0 \\ -u & 1 & 0 \\ -u & 0 & 1 \end{bmatrix}, \ \boldsymbol{H} = \begin{bmatrix} 0 & l & 1-l \\ c^2 - \frac{\bar{Q}_1^2}{A^2} & 2\frac{\bar{Q}_1}{A} - u & 0 \\ c^2 - \frac{\bar{Q}_2^2}{A^2} & 0 & 2\frac{\bar{Q}_2}{A} - u \end{bmatrix}, \tag{43}$$

where $l = l_{\frac{3}{2}}$, $u = u_{x,\frac{3}{2}}$, $Q_1 = l\bar{Q}_1$ and $Q_2 = (1-l)\bar{Q}_2$. System (42) is identical to the quasi-linear strictly hyperbolic system obtained in [6] for the two layers shallow water model with mass exchange. Therefore, the two layers system (41) is also strictly hyperbolic.

3.3. Multiring system of equations

In [6], the authors have studied the hyperbolicity of the multilayer shallow water system with mass exchange. They performed numerous numerical tests showing that for a given number of layers, the multilayer system is hyperbolic when small shear flows are considered. In regions of high shear, some eigenvalues can become complex and lead to the development of an Kelvin-Helmotz-like instability [4]. This behavior is expected as the RNS-P equations (1) are not a system of conservation laws. By analogy, this analysis is valid for the multiring system of equation (23) and we assume that in physiological conditions the multiring system (23) is hyperbolic.

4. Numerical methods

For simplicity, we rewrite system (23) in the following vectorial form:

$$\frac{\partial \boldsymbol{U}}{\partial t} + \frac{\partial}{\partial x}\left[\boldsymbol{F}\left(\boldsymbol{U}\right)\right] = \boldsymbol{S_M}\left(\boldsymbol{U}\right) + \boldsymbol{S_\nu}\left(\mathbf{U}\right) + \boldsymbol{S_T}\left(\boldsymbol{U}\right), \tag{44}$$

where:

$$\boldsymbol{U} = \begin{bmatrix} A \\ Q_1 \\ \vdots \\ Q_{N_r} \end{bmatrix}, \quad \boldsymbol{F}\left(\boldsymbol{U}\right) = \begin{bmatrix} F_A \\ F_{Q_1} \\ \vdots \\ F_{Q_{N_r}} \end{bmatrix}, \tag{45}$$

and:

$$\boldsymbol{S_M}\left(\boldsymbol{U}\right) = \begin{bmatrix} 0 \\ S_{M,1} \\ \vdots \\ S_{M,N_r} \end{bmatrix}, \ \boldsymbol{S_\nu}\left(\boldsymbol{U}\right) = \begin{bmatrix} 0 \\ S_{\nu,1} \\ \vdots \\ S_{\nu,N_r} \end{bmatrix}, \ \boldsymbol{S_T}\left(\boldsymbol{U}\right) = S_T \begin{bmatrix} 0 \\ l_1 \\ \vdots \\ l_{N_r} \end{bmatrix}. \tag{46}$$

The structure of the multiring system of equation (44) as a system of balance laws naturally leads us to propose a *finite volume* numerical scheme to obtain an approximate solution of the multiring system of equations (44). Doing so, we assure that the numerical scheme is robust, conservative and shock-capturing and that the numerical solution is positive if the chosen numerical flux preserves the positivity of the solution.

4.1. Problem splitting

The first step towards obtaining a numerical approximation of the solution of the multiring system of equations (44) in the *finite volume* framework is to discretize both the temporal and spatial domains. We first divide the time domain using a constant time step Δt and the discrete times are defined as:

$$t^n = n\Delta t, \quad n \in \mathbb{N}. \tag{47}$$

We note $\boldsymbol{U^n} = \boldsymbol{U}\left(t^n\right)$.

We then introduce a mesh in the axial direction and divide the length L of the artery in a series of cells C_i defined as:

$$C_i = \left[x_{i-\frac{1}{2}},\, x_{i+\frac{1}{2}}\right] = \left[\left(i-1\right)\Delta x,\, i\Delta x\right], \quad \text{for} \quad i = 1, ..., N_x, \tag{48}$$

where Δx is the cell size, supposed constant for simplicity, and $L = N_x \Delta x$.

Finally, we discretize the multiring system of equations (44) using a time splitting method:

$$\frac{\boldsymbol{U^*} - \boldsymbol{U^n}}{\Delta t} + \frac{\partial}{\partial x}\left[\boldsymbol{F}\left(\boldsymbol{U^n}\right)\right] = \boldsymbol{S_M}\left(\boldsymbol{U^n}\right) + \boldsymbol{S_T}\left(\boldsymbol{U^n}\right) \tag{49a}$$

$$\frac{\boldsymbol{U^{n+1}} - \boldsymbol{U^*}}{\Delta t} = \boldsymbol{S_\nu}\left(\boldsymbol{U^{n+1}}\right). \tag{49b}$$

Both the convective and viscous systems of equations (resp. eq. (49a) and (49b)) will be solved numerically in the following subsections.

4.2. Explicit convective numerical scheme

We first solve the convective system of equations (49a) using an explicit *finite volume* scheme, which includes the mass exchange source term $\boldsymbol{S_M}$ and the geometrical and mechanical source term $\boldsymbol{S_T}$.

Integrating the system of equations (49a) over the cell C_i, we obtain the explicit *finite volume* scheme:

$$\frac{\boldsymbol{U_i^*} - \boldsymbol{U_i^n}}{\Delta t} + \frac{1}{\Delta x}\left[\boldsymbol{F^n_{i+\frac{1}{2}}} - \boldsymbol{F^n_{i-\frac{1}{2}}}\right] = \boldsymbol{S^n_{M,i}} + \boldsymbol{S^n_{T,i}}, \tag{50}$$

where $\boldsymbol{U_i^n}$ is the space-average approximation of the vector $\boldsymbol{U}$ in the cell C_i at the time t^n:

$$\boldsymbol{U_i^n} \approx \frac{1}{\Delta x}\int_{C_i} \boldsymbol{U}\left(x, t^n\right) \mathrm{d}x. \tag{51}$$

The vector $\boldsymbol{F}^{\boldsymbol{n}}_{\boldsymbol{i+\frac{1}{2}}}$ is the two-points numerical flux vector, and corresponds to the numerical approximation of the flux vector $\boldsymbol{F}$ at interface $x_{i+\frac{1}{2}}$ of the cell C_i at time t^n:

$$\boldsymbol{F}^{\boldsymbol{n}}_{\boldsymbol{i+\frac{1}{2}}} = \boldsymbol{\mathcal{F}}\left(\boldsymbol{U}^{\boldsymbol{n}}_{\boldsymbol{i+\frac{1}{2},L}}, \boldsymbol{U}^{\boldsymbol{n}}_{\boldsymbol{i+\frac{1}{2},R}}\right) = \begin{bmatrix} \mathcal{F}_A\left(\boldsymbol{U}^{\boldsymbol{n}}_{\boldsymbol{i+\frac{1}{2},L}}, \boldsymbol{U}^{\boldsymbol{n}}_{\boldsymbol{i+\frac{1}{2},R}}\right) \\ \mathcal{F}_{Q_1}\left(\boldsymbol{U}^{\boldsymbol{n}}_{\boldsymbol{i+\frac{1}{2},L}}, \boldsymbol{U}^{\boldsymbol{n}}_{\boldsymbol{i+\frac{1}{2},R}}\right) \\ \vdots \\ \mathcal{F}_{Q_{N_r}}\left(\boldsymbol{U}^{\boldsymbol{n}}_{\boldsymbol{i+\frac{1}{2},L}}, \boldsymbol{U}^{\boldsymbol{n}}_{\boldsymbol{i+\frac{1}{2},R}}\right) \end{bmatrix}. \tag{52}$$

The flux $\mathcal{F}_A\left(\boldsymbol{U}^{\boldsymbol{n}}_{\boldsymbol{i+\frac{1}{2},L}}, \boldsymbol{U}^{\boldsymbol{n}}_{\boldsymbol{i+\frac{1}{2},R}}\right)$ can also be written as the sum of the contribution of each ring α:

$$\mathcal{F}_A\left(\boldsymbol{U}^{\boldsymbol{n}}_{\boldsymbol{i+\frac{1}{2},L}}, \boldsymbol{U}^{\boldsymbol{n}}_{\boldsymbol{i+\frac{1}{2},R}}\right) = \sum_{j=1}^{N_r} \mathcal{F}_{A_j}\left(\boldsymbol{U}^{\boldsymbol{n}}_{\boldsymbol{i+\frac{1}{2},L}}, \boldsymbol{U}^{\boldsymbol{n}}_{\boldsymbol{i+\frac{1}{2},R}}\right) \tag{53}$$

The choice of the vector function $\boldsymbol{\mathcal{F}}$ defines the numerical flux and thus the *finite volume* scheme. As we use only a first-order *finite volume* numerical scheme, the vectors $\boldsymbol{U}^{\boldsymbol{n}}_{\boldsymbol{i+\frac{1}{2},L}}$ and $\boldsymbol{U}^{\boldsymbol{n}}_{\boldsymbol{i+\frac{1}{2},R}}$ at the left and right of the interface $x_{i+\frac{1}{2}}$ of the cell C_i at time t^n are defined as:

$$\boldsymbol{U}^{\boldsymbol{n}}_{\boldsymbol{i+\frac{1}{2},L}} = \boldsymbol{U}^{\boldsymbol{n}}_{\boldsymbol{i}}, \qquad \boldsymbol{U}^{\boldsymbol{n}}_{\boldsymbol{i+\frac{1}{2},R}} = \boldsymbol{U}^{\boldsymbol{n}}_{\boldsymbol{i+1}}. \tag{54}$$

The vectors $\boldsymbol{S}^{\boldsymbol{n}}_{\boldsymbol{M,i}}$ and $\boldsymbol{S}^{\boldsymbol{n}}_{\boldsymbol{T,i}}$ correspond respectively to the discretization of the mass exchange source term $\boldsymbol{S_M}\left(\boldsymbol{U}^{\boldsymbol{n}}_{\boldsymbol{i}}\right)$ and of the geometrical and mechanical source term $\boldsymbol{S_T}\left(\boldsymbol{U}^{\boldsymbol{n}}_{\boldsymbol{i}}\right)$ and will be specified in the following subsections.

4.2.1. Kinetic flux

As shown previously, there is no analytic expression for the eigenvalues of the multiring system of equations (44). We therefore choose to use a kinetic flux function, which does not require the computation of the eigenstructure of the system (44). Other approaches are possible, see [24, 4]. A review of the kinetic method applied to different systems of equations can be found in [10] and more particularly to the 1D blood flow system in [3] and to the multilayer shallow water system with mass exchange in [6]. In the following, we briefly present the derivation of the expression of the kinetic vector function $\boldsymbol{\mathcal{F}}$ for the multiring system of equations (44).

According to kinetic theory, the vector function $\boldsymbol{\mathcal{F}}$ is defined as:

$$\boldsymbol{\mathcal{F}}\left(\boldsymbol{U_L}, \boldsymbol{U_R}\right) = \boldsymbol{\mathcal{F}}^+\left(\boldsymbol{U_L}\right) + \boldsymbol{\mathcal{F}}^-\left(\boldsymbol{U_R}\right), \tag{55}$$

where $\boldsymbol{\mathcal{F}}^+\left(\boldsymbol{U}\right)$ and $\boldsymbol{\mathcal{F}}^-\left(\boldsymbol{U}\right)$ are:

$$\boldsymbol{\mathcal{F}}^+\left(\boldsymbol{U}\right) = \begin{bmatrix} \sum_{j=1}^{N_r} \mathcal{F}^+_{A_j}\left(\boldsymbol{U}\right) \\ \mathcal{F}^+_{Q_1}\left(\boldsymbol{U}\right) \\ \vdots \\ \mathcal{F}^+_{Q_{N_r}}\left(\boldsymbol{U}\right) \end{bmatrix}, \quad \boldsymbol{\mathcal{F}}^-\left(\boldsymbol{U}\right) = \begin{bmatrix} \sum_{j=1}^{N_r} \mathcal{F}^-_{A_j}\left(\boldsymbol{U}\right) \\ \mathcal{F}^-_{Q_1}\left(\boldsymbol{U}\right) \\ \vdots \\ \mathcal{F}^-_{Q_{N_r}}\left(\boldsymbol{U}\right) \end{bmatrix}. \tag{56}$$

The fluxes $\mathcal{F}^{\pm}_{A_\alpha}\left(\boldsymbol{U}\right)$ and $\mathcal{F}^{\pm}_{Q_\alpha}\left(\boldsymbol{U}\right)$ in each ring α are defined as:

$$\begin{aligned} \begin{bmatrix} \mathcal{F}^+_{A_\alpha}\left(\boldsymbol{U}\right) \\ \mathcal{F}^+_{Q_\alpha}\left(\boldsymbol{U}\right) \end{bmatrix} &= \int_{\xi \geq 0} \xi \begin{bmatrix} 1 \\ \xi \end{bmatrix} M_\alpha\left(A, \xi - u_\alpha\right) \mathrm{d}\xi \\ \begin{bmatrix} \mathcal{F}^-_{A_\alpha}\left(\boldsymbol{U}\right) \\ \mathcal{F}^-_{Q_\alpha}\left(\boldsymbol{U}\right) \end{bmatrix} &= \int_{\xi \leq 0} \xi \begin{bmatrix} 1 \\ \xi \end{bmatrix} M_\alpha\left(A, \xi - u_\alpha\right) \mathrm{d}\xi. \end{aligned} \tag{57}$$

The function M_α is the kinetic Maxwellian, or so-called *Gibbs equilibrium*, and represents a distribution function of the microscopic particle velocity $\xi \in \mathbb{R}$ in the ring α:

$$M_\alpha\left(A, \xi - u_\alpha\right) = \frac{l_\alpha A}{\tilde{c}} \chi\left(\frac{\xi - u_\alpha}{\tilde{c}}\right), \tag{58}$$

where:

$$\tilde{c} = \sqrt{\frac{K}{3\rho}\sqrt{A}}. \tag{59}$$

We choose the function χ as:

$$\chi(w) = \begin{cases} \dfrac{1}{2\sqrt{3}} & \text{if } |w| \leq \sqrt{3} \\ 0 & \text{else.} \end{cases} \tag{60}$$

Injecting the expressions of the functions χ and M_α in the definition of the fluxes (57), we obtain after some computation the expressions for the fluxes $\mathcal{F}^{\pm}_{A_\alpha}(\boldsymbol{U})$ and $\mathcal{F}^{\pm}_{Q_\alpha}(\boldsymbol{U})$ in each ring α:

$$\begin{aligned} \begin{bmatrix} \mathcal{F}^{+}_{A_\alpha}(\boldsymbol{U}) \\ \mathcal{F}^{+}_{Q_\alpha}(\boldsymbol{U}) \end{bmatrix} &= \frac{l_\alpha A}{2\sqrt{3}\tilde{c}} \begin{bmatrix} \frac{1}{2}\left(\left(\xi^{+}_{p,\alpha}\right)^2 - \left(\xi^{+}_{m,\alpha}\right)^2\right) \\ \frac{1}{3}\left(\left(\xi^{+}_{p,\alpha}\right)^3 - \left(\xi^{+}_{m,\alpha}\right)^3\right) \end{bmatrix} \\ \begin{bmatrix} \mathcal{F}^{-}_{A_\alpha}(\boldsymbol{U}) \\ \mathcal{F}^{-}_{Q_\alpha}(\boldsymbol{U}) \end{bmatrix} &= \frac{l_\alpha A}{2\sqrt{3}\tilde{c}} \begin{bmatrix} \frac{1}{2}\left(\left(\xi^{-}_{p,\alpha}\right)^2 - \left(\xi^{-}_{m,\alpha}\right)^2\right) \\ \frac{1}{3}\left(\left(\xi^{-}_{p,\alpha}\right)^3 - \left(\xi^{-}_{m,\alpha}\right)^3\right) \end{bmatrix}, \end{aligned} \tag{61}$$

with:

$$\begin{cases} \xi^{+}_{p,\alpha} = \max\left(0, u_\alpha + \sqrt{3}\tilde{c}\right), & \xi^{+}_{m,\alpha} = \max\left(0, u_\alpha - \sqrt{3}\tilde{c}\right) \\ \xi^{-}_{p,\alpha} = \min\left(0, u_\alpha + \sqrt{3}\tilde{c}\right), & \xi^{-}_{m,\alpha} = \min\left(0, u_\alpha - \sqrt{3}\tilde{c}\right). \end{cases} \tag{62}$$

4.2.2. Mass exchange source term

We define the discrete mass exchange source term $\boldsymbol{S^n_{M,i}}$ as:

$$\boldsymbol{S^n_{M,i}} = \begin{bmatrix} 0 \\ u^n_{\frac{3}{2},i} G^n_{\frac{3}{2},i} \\ \vdots \\ u^n_{\alpha+\frac{1}{2},i} G^n_{\alpha+\frac{1}{2},i} - u^n_{\alpha-\frac{1}{2},i} G^n_{\alpha-\frac{1}{2},i} \\ \vdots \\ -u^n_{N_r-\frac{1}{2},i} G^n_{N_r-\frac{1}{2},i} \end{bmatrix}. \tag{63}$$

Following [6] and by analogy with expression (26), we compute $G^n_{\alpha+\frac{1}{2},i}$ in each ring α as:

$$\begin{aligned} G^n_{\alpha+\frac{1}{2},i} = \quad & \frac{1}{\Delta x} \sum_{j=1}^{\alpha} \left\{ \left[\mathcal{F}_{A_j}\left(\boldsymbol{U^n_{i+\frac{1}{2},L}}, \boldsymbol{U^n_{i+\frac{1}{2},R}}\right) - \mathcal{F}_{A_j}\left(\boldsymbol{U^n_{i-\frac{1}{2},L}}, \boldsymbol{U^n_{i-\frac{1}{2},R}}\right) \right] - \right. \\ & \left. l_j \left[\mathcal{F}_{A}\left(\boldsymbol{U^n_{i+\frac{1}{2},L}}, \boldsymbol{U^n_{i+\frac{1}{2},R}}\right) - \mathcal{F}_{A}\left(\boldsymbol{U^n_{i-\frac{1}{2},L}}, \boldsymbol{U^n_{i-\frac{1}{2},R}}\right) \right] \right\}. \end{aligned} \tag{64}$$

We define $u^n_{\alpha+\frac{1}{2},i}$ in an upwind manner:

$$u^n_{\alpha+\frac{1}{2},i} = \begin{cases} u^n_{\alpha,i} & \text{if} \quad G^n_{\alpha+\frac{1}{2},i} \leq 0 \\ u^n_{\alpha+1,i} & \text{if} \quad G^n_{\alpha+\frac{1}{2},i} > 0. \end{cases} \tag{65}$$

This choice is motivated by the analysis of expression (11) for the mass exchange term $G_{\alpha+\frac{1}{2}}$. Indeed, $G_{\alpha+\frac{1}{2}} > 0$ if the cross-sectional area $\pi R^2_{\alpha+\frac{1}{2}}$ increases with time or if the interface velocity $u_{r,\alpha+\frac{1}{2}} < 0$. In both cases, from the perspective of the interface $R_{\alpha+\frac{1}{2}}$, the flow is coming from the upper ring $\alpha+1$ and the upwind velocity is therefore $u_{x,\alpha+1}$.

4.2.3. Hydrostatic reconstruction of the source term $\mathbf{S_T}$

The considered kinetic flux function does not take into account the geometrical and mechanical source term $\boldsymbol{S_T}$, which results from axial variations of the cross-sectional area at rest A_0 or the arterial rigidity K. This source term must be treated using a well-balanced method to prevent spurious oscillations of the numerical solution close to steady states [50, 8, 30, 31].

To that effect, we use the well-balanced hydrostatic reconstruction technique (HR for short) introduced in [5] for shallow water equations. This technique was then applied to blood flow equations in [19, 18] and to

the multilayer shallow water system with mass exchange in [6]. Through a reconstruction of the conservative variables, HR allows to obtain a simple and efficient well-balanced numerical scheme given any *finite volume* numerical flux. We briefly recall the derivation of HR applied to the multiring system of equations (44).

We define the discrete geometrical and mechanical source term $\boldsymbol{S^n_{T,i}}$ as:

$$\boldsymbol{S^n_{T,i}} = S^n_{T,i} \begin{bmatrix} 0 \\ l_1 \\ \vdots \\ l_{N_r} \end{bmatrix}, \tag{66}$$

where $S^n_{T,i}$ is:

$$\begin{aligned} S^n_{T,i} \quad =& \frac{1}{3\rho\Delta x} \left[K^*_{i+\frac{1}{2}} \left[A^{*n}_{i+\frac{1}{2},L} \right]^{\frac{3}{2}} - K_{i+\frac{1}{2},L} \left[A^n_{i+\frac{1}{2},L} \right]^{\frac{3}{2}} \right. \\ & \left. - K^*_{i-\frac{1}{2}} \left[A^{*n}_{i-\frac{1}{2},R} \right]^{\frac{3}{2}} + K_{i-\frac{1}{2}} \left[A^n_{i-\frac{1}{2},R} \right]^{\frac{3}{2}} \right]. \end{aligned} \tag{67}$$

The reconstructed variables $A^{*n}_{i+\frac{1}{2},L}$, $A^{*n}_{i+\frac{1}{2},R}$ and $K^*_{i+\frac{1}{2}}$ are defined such that the steady states at rest are preserved as well as the positivity of the cross-sectional area A:

$$\begin{cases} A^{*n}_{i+\frac{1}{2},L} = \left(\dfrac{H^{*n}_{i+\frac{1}{2},L}}{K^*_{i+\frac{1}{2}}} \right)^2 \\ A^{*n}_{i+\frac{1}{2},R} = \left(\dfrac{H^{*n}_{i+\frac{1}{2},R}}{K^*_{i+\frac{1}{2}}} \right)^2 \\ K^*_{i+\frac{1}{2}} = \max \left(K_{i+\frac{1}{2},L}, K_{i+\frac{1}{2},R} \right), \end{cases} \tag{68}$$

with:

$$\begin{cases} H^{*n}_{i+\frac{1}{2},L} = \max \left(0, Z^*_{i+\frac{1}{2}} + \left[K\sqrt{A} \right]_{i+\frac{1}{2},L} - \left[K\sqrt{A_0} \right]_{i+\frac{1}{2},L} \right) \\ H^{*n}_{i+\frac{1}{2},R} = \max \left(0, Z^*_{i+\frac{1}{2}} + \left[K\sqrt{A} \right]_{i+\frac{1}{2},R} - \left[K\sqrt{A_0} \right]_{i+\frac{1}{2},R} \right) \\ Z^*_{i+\frac{1}{2}} = \min \left(\left[K\sqrt{A_0} \right]_{i+\frac{1}{2},L}, \left[K\sqrt{A_0} \right]_{i+\frac{1}{2},R} \right). \end{cases} \tag{69}$$

Finally, we obtain a well-balanced numerical scheme by replacing each occurrence of the conservative vectors $\boldsymbol{U^n_{i+\frac{1}{2},L}}$ and $\boldsymbol{U^n_{i+\frac{1}{2},R}}$ in the vector function $\boldsymbol{\mathcal{F}}$ by the reconstructed conservative vectors $\boldsymbol{U^{*n}_{i+\frac{1}{2},L}}$ and $\boldsymbol{U^{*n}_{i+\frac{1}{2},R}}$, defined as:

$$\boldsymbol{U^{*n}_{i+\frac{1}{2},L}} = \begin{bmatrix} A^{*n}_{i+\frac{1}{2},L} \\ Q^n_{1,i+\frac{1}{2},L} \\ \vdots \\ Q^n_{N_r,i+\frac{1}{2},L} \end{bmatrix}, \quad \boldsymbol{U^{*n}_{i+\frac{1}{2},R}} = \begin{bmatrix} A^{*n}_{i+\frac{1}{2},R} \\ Q^n_{1,i+\frac{1}{2},R} \\ \vdots \\ Q^n_{N_r,i+\frac{1}{2},R} \end{bmatrix}. \tag{70}$$

4.2.4. CFL condition

The stability of the convective numerical scheme is ensured if at each time t_n, the time step Δt verifies the following CFL (Courant, Friedrichs and Lewy) [17] condition:

$$\Delta t \leq \min_{i=1}^{N_x} \min_{j=1}^{N_r} \frac{l_j A^n_i \Delta x}{l_j A^n_i \left(|u^n_{j,i}| + \tilde{c}^n_i \right) + \Delta x \left(G^n_{j+\frac{1}{2},i} - G^n_{j-\frac{1}{2},i} \right)}. \tag{71}$$

This CFL condition ensures that the kinetic scheme preserves the positivity of the cross-sectional area A (for a detailed proof see [6]). Note that its more restrictive than the classical CFL condition used in 1D models as the flow can now exit the ring through both its axial and radial interfaces.

4.3. Implicit viscous numerical scheme

We now solve the viscous system of equations (49b) using an implicit numerical scheme. The implicit form of the scheme is chosen for stability reasons.

Integrating the system of equations (49b) over the cell C_i, we obtain the following implicit viscous numerical scheme:

$$\frac{\boldsymbol{U_i^{n+1}} - \boldsymbol{U_i^*}}{\Delta t} = \boldsymbol{S_{\nu,i}^{n+1}}, \tag{72}$$

where $\boldsymbol{U_i^*}$ is the solution of the system of equations (50) and $\boldsymbol{S_{\nu,i}^{n+1}}$ is the discretization of the viscous source term $\boldsymbol{S_\nu}\left(\boldsymbol{U_i^{n+1}}\right)$ and writes:

$$\boldsymbol{S_{\nu,i}^{n+1}} = \begin{bmatrix} 0 \\ S_{\nu,1,i}^{n+1} \\ \vdots \\ S_{\nu,N_r,i}^{n+1} \end{bmatrix}. \tag{73}$$

In each ring α of the cell C_i at time t^{n+1}, we define $S_{\nu,\alpha,i}^{n+1}$ as the discrete analog of $S_{\nu,\alpha}$ (13). To compute $S_{\nu,\alpha,i}^{n+1}$, we use a centered *finite difference* discretization of the term $\left[r\frac{\partial u_x}{\partial r}\right]_{R_{\alpha+\frac{1}{2}}}$:

$$\left[r\frac{\partial u_x}{\partial r}\right]_{R_{\alpha+\frac{1}{2}}} = J_{r,\alpha}\left[u_{\alpha+1,i}^{n+1} - u_{\alpha,i}^{n+1}\right] \quad \text{for} \quad \alpha = 1, \ldots, N_r - 1, \tag{74}$$

where:

$$J_{r,\alpha} = 2\frac{\sum_{j=1}^{\alpha} l_{r,j}}{l_{r,\alpha} + l_{r,\alpha+1}}. \tag{75}$$

At the interfaces $R_{\frac{1}{2}}$ and $R_{N_r+\frac{1}{2}}$, the previous discretization (74) of $\left[r\frac{\partial u_x}{\partial r}\right]$ is not possible and the boundary conditions (19) and (21) must be taken into account. At the ring interface $r_{\frac{1}{2}}$, the axisymmetric boundary condition (19) imposes that:

$$\left[r\frac{\partial u_x}{\partial r}\right]_{R_{\frac{1}{2}}} = 0. \tag{76}$$

To express $\left[r\frac{\partial u_x}{\partial r}\right]_{R_{N_r+\frac{1}{2}}}$ using only the conservative vector $\boldsymbol{U}$, we first perform the following asymptotic expansion of $u_x(x,r,t)$ in the ring N_r:

$$u_x(x,r,t) = u_x\left(x, R_{N_r+\frac{1}{2}}, t\right) + \left[r - R_{N_r+\frac{1}{2}}\right]\frac{\partial u_x}{\partial r}|_{R_{N_r+\frac{1}{2}}} + O\left(\left[R_{N_r+\frac{1}{2}} - r\right]^2\right). \tag{77}$$

Neglecting the higher-order terms and using the no-slip boundary condition (21), we obtain the following expression:

$$u_x(x,r,t) \approx \left[r - R_{N_r+\frac{1}{2}}\right]\frac{\partial u_x}{\partial r}|_{R_{N_r+\frac{1}{2}}}. \tag{78}$$

We then integrate the previous expression over the cross-sectional area of the ring N_r and we obtain:

$$\left[r\frac{\partial u_x}{\partial r}\right]_{R_{N_r+\frac{1}{2}}} = J_{r,\nu}\frac{Q_{N_r,i}^{n+1}}{A_i^{n+1}}, \tag{79}$$

with:

$$J_{r,\nu} = \frac{1}{-\frac{1}{3} + \left[1 - l_{r,N_r}\right]^2 - \frac{2}{3}\left[1 - l_{r,N_r}\right]^3}. \tag{80}$$

It is important to note that the discretization (79) of $\left[r\frac{\partial u_x}{\partial r}\right]_{R_{N_r+\frac{1}{2}}}$ imposes the no-slip boundary condition (21) at the wall, which is the natural boundary condition for viscous flows.

Finally, noticing that the first component of the source term $\boldsymbol{S_\nu}$ is zero, we obtain the following trivial solution of the system of equations (49b) for the first component of $\boldsymbol{U_i^{n+1}}$:

$$A_i^{n+1} = A_i^*, \quad \text{for} \quad i = 1, ..., N_x. \tag{81}$$

We can therefore rewrite the implicit viscous scheme (72) in the following matrix form:

$$\left[\boldsymbol{I} + \Delta t \boldsymbol{M}^*_{\boldsymbol{\nu,i}}\right] \begin{bmatrix} Q^{n+1}_{1,i} \\ \vdots \\ Q^{n+1}_{\alpha,i} \\ \vdots \\ Q^{n+1}_{N_r,i} \end{bmatrix} = \begin{bmatrix} Q^{*}_{1,i} \\ \vdots \\ Q^{*}_{\alpha,i} \\ \vdots \\ Q^{*}_{N_r,i} \end{bmatrix}, \tag{82}$$

where $\boldsymbol{I}$ is the identity matrix and $\boldsymbol{M^*_{\nu,i}}$ is the following tridiagonal matrix:

$$\boldsymbol{M^*_{\nu,i}} = \frac{2\pi\nu}{A^*_i} \begin{bmatrix} \frac{J_{r,1}}{l_1} & -\frac{J_{r,1}}{l_2} & 0 & \dots & 0 \\ \ddots & \ddots & \ddots & \ddots & \vdots \\ 0 & -\frac{J_{r,\alpha-1}}{l_{\alpha-1}} & \frac{J_{r,\alpha-1}+J_{r,\alpha}}{l_\alpha} & -\frac{J_{r,\alpha}}{l_{\alpha+1}} & 0 \\ \vdots & \ddots & \ddots & \ddots & \ddots \\ 0 & \dots & 0 & -\frac{J_{r,N_r-1}}{l_{N_r-1}} & \frac{J_{r,N_r-1}}{l_{N_r}} - J_{r,\nu} \end{bmatrix}. \tag{83}$$

We then invert the system of equations (82) using the Thomas algorithm [62], well-suited for solving tridiagonal matrix systems.

Next, we provide algorithms to impose classical inlet and outlet boundary conditions for blood flow.

5. Boundary conditions

As we compute subcritical solutions of system (23), boundary conditions are required at both ends of the computational domain, in the inlet and outlet ghost cells of the artery, respectively noted C_{in} and C_{out}. In both cells C_{in} and C_{out}, the corresponding conservative vectors $\boldsymbol{U^n_{in}}$ and $\boldsymbol{U^n_{out}}$ must be prescribed in order to update the numerical solution from time t^n to time t^{n+1} in each cell C_i of the computational domain. We propose here algorithms to impose boundary conditions in the inlet and outlet ghost cells of the artery. As the implementation of inlet and outlet boundary conditions is very similar, we describe only the derivation of the inlet boundary conditions.

5.1. Imposed flow rate Q

We wish to impose the flow rate $Q^n_{e,\alpha}$ at the interface between the first cell C_1 and the inlet ghost cell C_{in} of each ring α, namely:

$$\mathcal{F}_{A_\alpha}\left(\boldsymbol{U^n_{in}}, \boldsymbol{U^n_1}\right) = Q^n_{e,\alpha} \quad \text{for} \quad \alpha = 1, ..., N_r. \tag{84}$$

Following the methodology proposed in [11] and taking advantage of the fact that the kinetic flux function $\mathcal{F}_{\mathcal{A}_\alpha}$ can be split in two, equation (84) can be expressed as:

$$\mathcal{F}^+_{A_\alpha}\left(\boldsymbol{U^n_{in}}\right) + \mathcal{F}^-_{A_\alpha}\left(\boldsymbol{U^n_1}\right) = Q^n_{e,\alpha} \quad \text{for} \quad \alpha = 1, ..., N_r. \tag{85}$$

To ensure the stability of the scheme, the condition (85) in each ring α is imposed in an upwind manner. Consequently, we define the quantity:

$$a = \sum_{\alpha=1}^{N_r} Q^n_{e,\alpha} - \mathcal{F}^-_{A_\alpha}\left(\boldsymbol{U^n_1}\right), \tag{86}$$

and distinguish two cases:

- If $a \leq 0$, the dominant part of the information is coming from inside the computational domain. As we are performing an upwind evaluation of the inlet boundary condition, we impose:

$$\begin{aligned} &\mathcal{F}^+_A\left(\boldsymbol{U^n_{in}}\right) = 0 \\ &\mathcal{F}^+_{Q_\alpha}\left(\boldsymbol{U^n_{in}}\right) = 0 \quad \text{for} \quad \alpha = 1, ..., N_r. \end{aligned} \tag{87}$$

- If $a > 0$, the dominant part of the information is coming from outside the computational domain. In this case, we impose:

$$\begin{aligned} &\mathcal{F}^{+}_{A_\alpha}\left(\boldsymbol{U_{in}^n}\right) = Q^n_{e,\alpha} - \mathcal{F}^{-}_{A_\alpha}\left(\boldsymbol{U_1^n}\right) \quad \text{for} \quad \alpha = 1, ..., N_r \\ &W_1\left(\boldsymbol{U_{in}^n}\right) = W_1\left(\boldsymbol{U_1^n}\right). \end{aligned} \tag{88}$$

  $W_1(\boldsymbol{U})$ is the 1D analog of the Riemann invariant $W_{1,\alpha}(\boldsymbol{U})$ in the ring α and characterizes the global outgoing characteristic. It writes:

$$W_1 = \frac{\sum_{\alpha=1}^{N_r} Q_\alpha}{A} - c. \tag{89}$$

  Similarly, we write $W_2(\boldsymbol{U})$ as:

$$W_2 = \frac{\sum_{\alpha=1}^{N_r} Q_\alpha}{A} + c. \tag{90}$$

$\boldsymbol{U_{in}^n}$ is obtained by solving either system (87) or system (88). This can be done using a classic Newton's method in a limited number of iterations.

5.2. Imposed cross-sectional area A

We wish to impose the cross-sectional area A_e^n in the inlet ghost cell C_{in}. Therefore, we set:

$$A^n_{in} = A^n_e. \tag{91}$$

To completely determine the inlet vector of conservative variables $\boldsymbol{U_{in}^n}$, we estimate the outgoing Riemann invariant $W_{1,\alpha}\left(\boldsymbol{U_{in}^n}\right)$ in the ring α as:

$$W_{1,\alpha}\left(\boldsymbol{U_{in}^n}\right) = W_{1,\alpha}\left(\boldsymbol{U_1^n}\right) \quad \text{for} \quad \alpha = 1, ..., N_r, \tag{92}$$

and using equations (39) and (40), we compute $W_{2,\alpha}\left(\boldsymbol{U_{in}^n}\right)$ and then $Q^n_{in,\alpha}$ in each ring α:

$$\begin{cases} W_{2,\alpha}\left(\boldsymbol{U_{in}^n}\right) = W_{1,\alpha}\left(\boldsymbol{U_{in}^n}\right) + 8c^n_{in} \\ Q^n_{in,\alpha} = l_\alpha A^n_{in} \dfrac{W_{1,\alpha}\left(\boldsymbol{U_{in}^n}\right) + W_{2,\alpha}\left(\boldsymbol{U_{in}^n}\right)}{2}. \end{cases} \tag{93}$$

5.3. Imposed reflection coefficient R_t

We wish to impose the reflection coefficient R_t in the inlet ghost cell C_{in}. The inlet reflection coefficient R_t is defined as:

$$W_2\left(\boldsymbol{U_{in}^n}\right) - W_2\left(\boldsymbol{U_{in}^0}\right) = -R_t\left[W_1\left(\boldsymbol{U_{in}^n}\right) - W_1\left(\boldsymbol{U_{in}^0}\right)\right], \tag{94}$$

and characterizes the proportion of the outgoing information reflected back into the computational domain. When we wish to remove any reflection of the outgoing information, we set $R_t = 0$. We first estimate the outgoing Riemann invariant $W_1\left(\boldsymbol{U_{in}^n}\right)$ as:

$$W_1\left(\boldsymbol{U_{in}^n}\right) = W_1\left(\boldsymbol{U_1^n}\right), \tag{95}$$

and using equation (94), we compute $W_2\left(\boldsymbol{U_{in}^n}\right)$ and then A^n_{in}:

$$A^n_{in} = \left(\frac{2\rho}{K_{in}}\right)^2 \left(\frac{W_2\left(\boldsymbol{U_{in}^n}\right) - W_1\left(\boldsymbol{U_{in}^n}\right)}{8}\right)^4. \tag{96}$$

Finally, we use the algorithm presented in the previous subsection to completely determine the inlet vector of conservative variables $\boldsymbol{U_{in}^n}$.

In the following sections, we perform a series of numerical tests to validate the multiring model (23), the numerical scheme and the boundary conditions previously described.

6. Linear examples in an elastic artery

6.1. The Womersley solution

In [68], Womersley proposed an analytic harmonic solution of the linearized Navier-Stokes equations which is also a solution of the linearized RNS-P equations (1). The Womersley solution is an important test case for numerical methods simulating blood flow in elastic arteries as it includes pulsatile effects, elastic deformation of the arterial wall and viscous dissipation. In [36, 15, 21], the authors used the Womersley solution in a rigid axisymmetric tube to validate their numerical method. In this section, we compute the Womersley solution in an elastic artery as a first validation case of the multiring model (23).

6.1.1. Linear harmonic solution

We briefly detail the derivation of the Womersley solution starting from the linear RNS-P system of equations:

$$\begin{cases} \dfrac{1}{r}\dfrac{\partial}{\partial r}\left[r u_r\right] + \dfrac{\partial u_x}{\partial x} = 0 & \text{(97a)} \\ \dfrac{\partial u_x}{\partial t} = -\dfrac{1}{\rho}\dfrac{\partial p}{\partial x} + \dfrac{\nu}{r}\dfrac{\partial}{\partial r}\left[r\dfrac{\partial u_x}{\partial r}\right] & \text{(97b)} \\ p\left(x,t\right). & \text{(97c)} \end{cases}$$

Following [68], we search for a harmonic solution of the axial velocity $u_x(x,r,t)$, the pressure $p\left(x,t\right)$ and the radius $R\left(x,t\right)$:

$$\begin{cases} u_x(x,r,t) = \hat{u}_x(r)e^{i(\omega t - kx)} \\ p\left(x,t\right) = p_0 + \hat{p}e^{i(\omega t - kx)} \\ R\left(x,t\right) = R_0\left(x\right) + \hat{R}e^{i(\omega t - kx)}, \end{cases} \tag{98}$$

with $\hat{R} \ll 1$. For simplicity we choose $p_0 = 0$. Injecting the expressions (98) in the linear momentum equation (97b), we obtain:

$$\frac{\partial^2 \hat{u}_x}{\partial r^2} + \frac{1}{r}\frac{\partial \hat{u}_x}{\partial r} - i\frac{\alpha^2}{R^2}\hat{u}_x = -\frac{i\omega}{\mu c}\hat{p}, \tag{99}$$

where α is the Womersley number and c is the wave celerity, respectively defined as:

$$\alpha = R\sqrt{\frac{\omega}{\nu}} \quad \text{and} \quad c = \frac{\omega}{k}. \tag{100}$$

The Womersley number α represents the relative importance of pulsatile effects with respect to viscous effects and is the relevant dimensionless number in this example. Combining both the homogeneous solution of equation (99), computed using the Bessel function J_0, and the particular solution of equation (99), we obtain the general solution of equation (99), using the no-slip boundary condition at the wall (21):

$$\hat{u}_x = \frac{\hat{p}}{\rho c}\left(1 - \frac{J_0\left(i^{\frac{3}{2}}\alpha\frac{r}{R}\right)}{J_0\left(i^{\frac{3}{2}}\alpha\right)}\right). \tag{101}$$

Using expression (101), we compute the flow rate Q and the wall shear stress (WSS) τ_w as:

$$Q = \hat{Q}e^{i(wt-kz)}, \quad \hat{Q} = \int_0^{2\pi}\int_0^R \hat{u}_x r \mathrm{d}r\mathrm{d}\theta = \pi R^2 \frac{\hat{p}}{\rho c}\left(1 - F_{10}\left(\alpha\right)\right), \tag{102}$$

and:

$$\tau_w = \hat{\tau}_w e^{i(wt-kz)}, \qquad \hat{\tau}_w = -\mu\frac{\partial u_x}{\partial r}|_{r=R} = i\frac{\nu\alpha^2}{2R}\frac{\hat{p}}{\rho c}F_{10}\left(\alpha\right), \tag{103}$$

where F_{10} is defined as:

$$F_{10}\left(\alpha\right) = \frac{2}{i^{\frac{3}{2}}\alpha}\frac{J_1(i^{\frac{3}{2}}\alpha)}{J_0(i^{\frac{3}{2}}\alpha)}. \tag{104}$$

Finally, after integrating the mass equation (97a) over the cross-sectional area of the artery, we obtain the following linearized expression for the wave celerity c:

$$c = \frac{\hat{p}}{\hat{R}}\frac{R_0}{2\rho}\left[1 - F_{10}\left(\alpha\right)\right]. \tag{105}$$

The inlet boundary condition imposes the value of either $\hat{p}$ or $\hat{R}$, which are linked through the elastic pressure law (18):

$$\frac{\hat{p}}{\hat{R}} = \sqrt{\pi} K. \tag{106}$$

Next, we compare the numerical solution of the multiring system of equations (23) to the linear harmonic Womersley solution presented previously.

6.1.2. Numerical results

We consider a straight artery initially at rest:

$$\begin{cases} A\left(x, t=0\right) = A_0 \\ Q_\alpha\left(x, t=0\right) = 0 \quad \text{for} \quad \alpha = 1, \ldots, N_r. \end{cases} \tag{107}$$

We impose at the inlet a sinusoidal oscillation of the pressure:

$$p\left(x=0, t\right) = \hat{p} \sin\left[2\pi \frac{t}{T_c}\right], \quad \hat{p} = \sqrt{\pi} K \hat{R}, \tag{108}$$

and at the outlet a zero reflection coefficient R_t to remove any backward traveling waves. The values of the geometrical and mechanical parameters describing the artery as well as those describing the inlet and outlet boundary conditions are presented in table 1 and are given in "cgs". The final time t_f is large enough to reach a periodic regime. The geometrical and mechanical parameters mimic physiological conditions and the value of $\hat{R}$ is small enough such that the linear approximation required to obtain the Womersley solution is valid.

L	R_0	K	ρ	μ	$\hat{R}$	R_t	T_c	t_f	α
200	1	10^4	1	$2\pi \frac{\rho}{T_c} \frac{R_0^2}{\alpha^2}$	10^{-3}	0	0.5	$12T_c$	$\{5, 20\}$

Table 1: *Elastic Womersley example. Geometrical and mechanical parameters describing the artery and the inlet and outlet boundary conditions, given in "cgs".*

For the sake of illustration, we consider only two different Womersley numbers, $\alpha = 5$ and $\alpha = 20$, chosen to respectively represent flow conditions in arterioles and large arteries. At small Womersley numbers ($\alpha = 5$), the viscous effect dominates, whereas at large Womersley numbers ($\alpha = 20$) the unsteady advection effect is dominant.

In figure 2, we plot the velocity profiles obtained in $x = 25$ at $t \in \{0.2, 0.4, 0.5, 0.7\}\, T_c + 11T_c$ for $\alpha = 5$ (fig. 2 left) and $\alpha = 20$ (fig. 2 right). We use $N_x = 1600$ cells and $N_r = 128$ rings. We observe that in both cases ($\alpha = 5$ and $\alpha = 20$) the Womersley and the multiring solutions are in good accord for each recorded time. Small discrepancies between both solutions appear near the maximums of the velocity due to the numerical dissipation of the kinetic scheme.

In figure 3, we represent the spatial evolution of the flow rate Q, the pressure p and the wall shear stress (WSS) τ_w obtained at time $t = 0.3T_c + 11T_c$ for $\alpha = 5$ (fig. 3 left) and $\alpha = 20$ (fig. 3 right). Once again, we use $N_x = 1600$ cells and $N_r = 128$ rings. For $\alpha = 20$, the Womersley and the multiring solutions overlap except at the local maximums and minimums of Q, p and τ_w, which are slightly dissipated by the numerical viscosity of the scheme. For $\alpha = 5$, both solutions match almost perfectly as the viscous dissipation is much larger than the numerical dissipation.

Next, we perform a convergence analysis in both the number of cells N_x and the number of rings N_r. In figure 4, we plot the L_2 spatial error between the Womersley and the multiring solutions as a function of the dimensionless number of cells $\bar{N}_x = \lambda N_x / L$, where λ is the wavelength of the pressure pulse, and of the dimensionless number of rings $\bar{N}_r = N_r / \alpha$ for $\alpha = 5$ (fig. 4 left) and $\alpha = 20$ (fig. 4 right). We focus only on the flow rate Q and the WSS τ_w taken at time $t = 0.3T_c + 11T_c$. For both $\alpha = 5$ and $\alpha = 20$, we observe that increasing $\bar{N}_x$ or $\bar{N}_r$ is not equivalent. For low values of $\bar{N}_x$, increasing $\bar{N}_r$ does not decrease the error significantly, whereas increasing $\bar{N}_x$ does. On the contrary, for high values of $\bar{N}_x$, increasing $\bar{N}_r$ significantly decreases the error, whereas increasing $\bar{N}_x$ does not. This behavior is expected as wave propagation in the axial direction is the dominant physical mechanism of the Womersley solution and can only be captured if a sufficient number of cells $\bar{N}_x$ is used. Only once a sufficient number of cells $\bar{N}_x$ is used can we increase the number of rings $\bar{N}_r$ to compute in detail the velocity profile. However, the behavior of the WSS τ_w for $\alpha = 20$ is different from the behavior of the other quantities. Indeed, the effect of increasing the number of rings $\bar{N}_r$ for low values

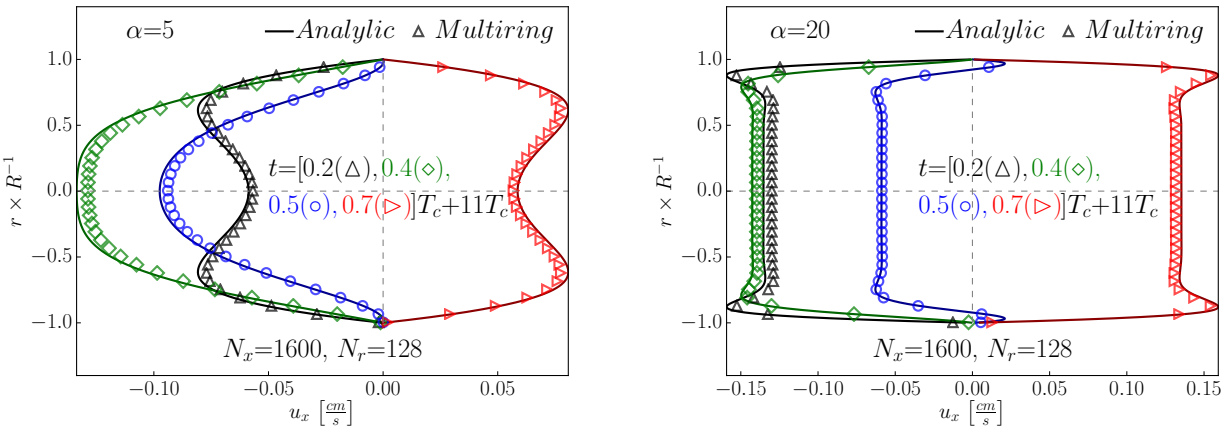

Figure 2: *Elastic Womersley example. Comparison between the velocity profiles obtained with the analytic Womersley solution (—) and with the multiring model using $N_x = 1600$ cells and $N_r = 128$ rings in $x = 25$ at times $t \in \{0.2\,(\Delta)\,,\ 0.4\,(\diamond)\,,\ 0.5\,(\circ)\,,\ 0.7\,(\triangleright)\}\,T_c + 11T_c$ for $\alpha = 5$ (left) and $\alpha = 20$ (right). We observe that the multiring solution agrees well with the analytic Womersley solution.*

of $\bar{N}_x$ is more significant than for the other quantities. This is due to the fact that for $\alpha = 20$, the boundary layer is thin, therefore increasing $\bar{N}_r$ immediately allows to better capture the viscous behavior of the flow and therefore the WSS τ_w. As a rule of thumbs, we observe that $\bar{N}_x = 500$ and $\bar{N}_r = 2$ is the minimum mesh and ring refinements to obtain an accurate description of the Womersley solution.

To conclude this analysis, we study three additional flow configurations where we increase the nonlinearity of the elastic Womersley solution by changing the amplitude of the wall perturbation $\hat{R}$. We choose $\hat{R} \in \left\{10^{-3},\ 10^{-2},\ 10^{-1},\ 3\times10^{-1}\right\}$. In figure 5, we plot snapshots of the spatial evolution of the axial velocity profile u_x in the artery at time $t = 0.3T_c + 11T_c$ obtained for $\alpha = 20$ and using $N_x = 1600$ cells and $N_r = 128$ rings. The values of the other geometrical and mechanical parameters describing the artery are identical to those of table 1. We observe that the multiring model (23) is able to compute with identical computational costs linear and nonlinear flow behaviors with small and large deformations of the arterial wall.

6.2. The steady linear elastic Poiseuille solution

In [29], the author proposed a steady analytic solution of the linear RNS-P equations (97) in an elastic artery. As the Poiseuille solution, it describes the steady balance between the pressure gradient and the viscous radial dissipation term:

$$\begin{cases} u\,(x,r) = \dfrac{2Q}{\pi R^2\,(x)}\left[1 - \left[\dfrac{r}{R\,(x)}\right]^2\right] \\ p\,(x) = p_0 + K\sqrt{\pi}\,[R\,(x) - R_0] \\ R\,(x) = \left[R^5\,(x=0) - \dfrac{40\nu Q}{\pi^{\frac{3}{2}}K}x\right]^{\frac{1}{5}} \\ Q = \dfrac{\pi^{\frac{3}{2}}K}{40\nu L}\left[R^5\,(x=0) - R^5\,(x=L)\right]. \end{cases} \tag{109}$$

In [15, 21], the authors used this solution to validate their numerical code solving the axisymmetric RNS-P equations (1). We reproduce here this solution using the multiring model (23).

We consider a straight artery initially at rest (eq. (107)). We impose the pressure gradient by setting at the inlet and outlet constant pressures consistent with the analytic solution (109):

$$\begin{cases} p\,(x=0) = p_0 + \sqrt{\pi}KR_0\hat{R} \\ p\,(x=L) = p_0 - \sqrt{\pi}KR_0\hat{R}. \end{cases} \tag{110}$$

For simplicity we set $p_0 = 0$. The values of the geometrical and mechanical parameters describing the artery as well as those describing the inlet and outlet boundary conditions are presented in table 2 and are given in "cgs". The final time t_f is large enough to reach a steady flow regime and the value of $\hat{R}$ is small enough such that the linear approximation required to obtain the elastic Poiseuille solution is valid.

L	R_0	K	ρ	μ	$\hat{R}$	t_f
10	1	$\frac{10^2}{\sqrt{\pi}}$	1	1	10^{-1}	20

Table 2: *Steady linear elastic Poiseuille example. Geometrical and mechanical parameters describing the artery and the inlet and outlet boundary conditions, given in "cgs".*

In figure 6, we plot the spatial evolution of the steady radius R (fig. 6 left) and the steady axial velocity profiles taken in $x \in \{0,\, 0.2,\, 0.4,\, 0.6,\, 0.8,\, 0.99\}\, L$ (fig. 6 right). We use $N_x = 800$ cells and $N_r = 64$ rings. We observe that for each recorded point the steady multiring numerical solution is in agreement with the steady analytic solution.

As this analytic solution is smooth enough, we perform a convergence analysis to determine the order of accuracy of the scheme. We consider the following mesh refinements $[N_x, N_r] \in \{[100, 8]\,, [200, 16]\,, [400, 32]\,, [800, 64]\}$ and focus only on the radius R for simplicity. In table 3, we compute the L_1, L_2 and L_∞ spatial errors between the analytic solution (109) and the steady numerical solution for the radius R. We observe that the numerical solution converges at order 1, which is the expected order of convergence.

N_x	N_r	$L_1(R)$	$O_{L_1(R)}$	$L_2(R)$	$O_{L_2(R)}$	$L_\infty(R)$	$O_{L_\infty(R)}$
100	8	1.29×10^{-3}	-	7.35×10^{-4}	-	5.36×10^{-4}	-
200	16	5.93×10^{-4}	-0.56	3.37×10^{-4}	-0.56	2.46×10^{-4}	-0.56
400	32	2.25×10^{-4}	-0.70	1.27×10^{-4}	-0.70	9.33×10^{-5}	-0.70
800	64	4.54×10^{-5}	-1.15	2.49×10^{-5}	-1.18	2.05×10^{-5}	-1.09

Table 3: *Steady linear elastic Poiseuille example. L_1, L_2 and L_∞ spatial errors between the steady analytic solution* (109) *and the steady multiring numerical solution for the radius R obtain using $[N_x, N_r] \in \{[100, 8]\,, [200, 16]\,, [400, 32]\,, [800, 64]\}$ cells and rings. We observe that the numerical solution converges at order 1, which is the expected order of convergence.*

In the two previous examples, we have shown that the multiring model (23) is able to accurately capture steady and unsteady linear blood flow in a straight artery. We are therefore confident that the multiring model (23) can compute all relevant linear flow features encountered in large straight axisymmetric elastic arteries. However, the RNS-P system of equations (1) is a rich dynamical system and is not limited to describing linear harmonic and steady solutions in elastic arteries. In the following sections, we will continue to validate the multiring model, the numerical scheme and the boundary conditions using nonlinear steady examples in rigid arteries with varying geometrical and mechanical properties.

7. Nonlinear examples in a rigid artery

7.1. Nonlinear transition from a flat to a Poiseuille velocity profile

In [37], the authors studied the behavior of the RNS-P system of equations (1) when computing steady flows in a rigid axisymmetric cylinder. They showed that it is able to describe the steady spatial transition from the Blasius [53] to the Poiseuille flow regime, starting from a flat velocity profile at the inlet and evolving towards a fully developed Poiseuille velocity profile at the outlet. We reproduce here this phenomenon using the multiring model (23). The relevant dimensionless number in this example is the Reynolds number $R_{e,R}$, defined as:

$$R_{e,R} = \frac{u_{x_{|x=0}} R_{|x=0}}{\nu}, \tag{111}$$

and used to determine the relevant length and time scales in order to observe the steady spatial transition from the Blasius to the Poiseuille flow regime. Details on the determination of theses scales can be found in [37].

We consider a straight artery initially at rest (eq. (107)). We impose at the inlet a steady velocity profile. We can not impose a flat velocity profile as it is not compatible with the no-slip boundary condition at the wall (21). Therefore we impose at the inlet a Von Kármán-Pohlhausen velocity profile [46], describing a fourth-order approximation of the axial velocity profile in the viscous boundary layer:

$$u_x\,(x = 0, r, t) = U_{in}\; \phi_{Pohlhausen}\,(r)\,, \tag{112}$$

where:

$$\phi_{Pohlhausen}(r) = \begin{cases} \dfrac{1-[1-\eta]^3\left[1+\left[1+\frac{\Delta}{6}\right]\eta\right]}{\frac{1}{30}\left[30-3\left[6+\frac{\Delta}{6}\right]\delta_{BL}+\left[4+\frac{\Delta}{6}\right]\delta_{BL}^2\right]} & \text{if } \eta < 1 \\ \dfrac{1}{\frac{1}{30}\left[30-3\left[6+\frac{\Delta}{6}\right]\delta_{BL}+\left[4+\frac{\Delta}{6}\right]\delta_{BL}^2\right]} & \text{if } \eta \geq 1, \end{cases} \tag{113}$$

with $\Delta = 12$ and $\eta = \left[1-\frac{r}{R(x,t)}\right]/\delta_{BL}$. The parameter δ_{BL} is the estimated width of the boundary layer, that we choose here equal to $\delta_{BL} = l_{r,N_r} + l_{r,N_r-1}$. We impose at the outlet a zero reflection coefficient R_t to remove any backward traveling waves. The values of the geometrical and mechanical parameters describing the artery as well as those describing the inlet and outlet boundary conditions are presented in table 4 and are given in "cgs". The final time t_f is large enough to reach a steady flow regime. The geometrical and mechanical parameters mimic physiological conditions at the root of the aorta, where $R_{e,R} \approx 100$.

L	R_0	K	ρ	μ	U_{in}	R_t	t_f	$R_{e,R}$
$0.25\ R_{e,R}R_{\|x=0}$	1	10^7	1	$\rho\frac{U_{in}R_{\|x=0}}{R_{e,R}}$	100	0	$0.5\frac{R_{e,R}R_{\|x=0}}{U_{in}}$	100

Table 4: *Steady rigid Poiseuille example. Geometrical and mechanical parameters describing the artery and the inlet and outlet boundary conditions, all given in "cgs".*

As the multiring model (23) is intrinsically elastic, it is not possible to exactly simulate the flow of blood in a rigid cylinder. Nevertheless, by artificially increasing the arterial wall rigidity K (here $K = 10^7$), we penalize the wall's displacement and place ourselves in a quasi-rigid wall configuration.

To assess the quality of the multiring numerical results, we compare them to those of the steady numerical code presented in [37]. This steady code was used to solve the steady RNS-P system of equations (1) in a rigid tube and compared well with the results of an integral interactive boundary layer (IBL) code. In the following examples, all results of the steady code used as reference solutions are obtained using $N_x = 50000$ cells in the axial direction and $N_r = 1000$ cells in the radial direction.

In figure 7, we plot the steady spatial evolution of the centerline velocity $u_{x_{|r=0}}$ (fig. 7 left) and of the pressure p (fig. 7 right). We use $N_x \in \{800, 1600, 3200\}$ cells and $N_r = 32$ rings. We observe that as we increase the number of cells N_x, the steady multiring numerical solution converges towards the steady numerical solution and is able to describe the spatial transition from a flat velocity profile to a Poiseuille velocity profile. The number of cells N_x required to match the steady solution is relatively high due to the numerical dissipation of the kinetic scheme and since the transition from of flat to a Poiseuille velocity profile is a nonlinear phenomenon occurring on a short length scale (between $x = 0$ and $x = 0.15R_{e,R}R_{|x=0}$).

In figure 8, we represent the steady velocity profiles taken in $x \in \{0.005, 0.01, 0.025, 0.05, 0.1, 0.2\}\ R_{e,R}R_{|x=0}$. We use $N_x \in \{800, 3200\}$ cells and $N_r = 32$ rings. For each recorded position, the steady multiring numerical velocity profiles converge towards the steady numerical velocity profiles as we increase the number of cells N_x. These results are coherent with the results presented in figure 7.

7.2. Rigid wall stenosis and aneurysm

Stenoses and aneurysms are commonly encountered pathologies and correspond respectively to local constrictions and expansions of the radius at rest of the artery. The flow patterns in rigid stenoses and aneurysms have been studied by many authors [66, 67, 45, 20, 70, 64]. In [37], the authors computed the numerical solution of the steady RNS-P system of equations (1) in an axisymmetric rigid artery presenting a stenosis. They used the steady code presented in the previous section and were able to compute flow recirculations in case of severe stenoses. We use here the multiring model (23) to compute the steady flow in a rigid stenosis and in a rigid aneurysm. As in the previous section, the relevant dimensionless number is the Reynolds number $R_{e,R}$ (eq. (111)).

We consider an artery initially at rest (eq. (107)). We impose at the inlet a steady Poiseuille velocity profile:

$$u_x(x=0,r,t) = 2U_{in}\left[1-\frac{r^2}{R(x,t)^2}\right], \tag{114}$$

and at the outlet a zero reflection coefficient R_t to remove any backward traveling waves. The values of the geometrical and mechanical parameters describing the artery as well as those describing the inlet and outlet

boundary conditions are presented in table 5 and are given in "cgs". The final time t_f is large enough to reach a steady flow regime. The geometrical and mechanical parameters mimic physiological conditions at the root of the aorta, where $R_{e,R} \approx 100$. The stenosis and aneurysm considered here are described by the following variation of the radius at rest R_0:

$$R_0(x) = \begin{cases} R_0 & \text{if } x < x_s \text{ or } x > x_f \\ R_0\left(1 + \dfrac{\Delta R}{2}\left[1 + \cos\left(\pi + 2\pi\dfrac{x - x_s}{x_f - x_s}\right)\right]\right) & \text{if } x_s \leq x \geq x_f. \end{cases} \tag{115}$$

We choose $x_s = \frac{L}{5}$ and $x_f = \frac{3L}{5}$ to satisfy the long-wave hypothesis. We set $\Delta R = -0.4$ to define the stenosis and $\Delta R = +0.4$ to define the aneurysm. We artificially increase the arterial wall rigidity K (here $K = 10^7$) to penalize the wall's displacement and place ourselves in a quasi-rigid wall configuration.

L	R_0	K	ρ	μ	U_{in}	R_t	t_f	$R_{e,R}$
$0.25\ R_{e,R}R_{\|x=0}$	1	10^7	1	$\rho\frac{U_{in}R_{\|x=0}}{R_{e,R}}$	100	0	$0.5\frac{R_{e,R}R_{\|x=0}}{U_{in}}$	100

Table 5: *Steady rigid stenosis and aneurysm examples. Geometrical and mechanical parameters describing the artery and the inlet and outlet boundary conditions, all given in "cgs".*

We compare the results of the multiring model (23) to those of the steady numerical code presented in [37]. In [16], this steady code was used to solve the steady RNS-P system of equations (1) in a rigid stenosis and compared well to the results of a finite element code for the incompressible Navier-Stokes equations. In the following examples, all results of the steady code used as reference solutions are obtained using $N_x = 50000$ cells in the axial direction and $N_r = 1000$ cells in the radial direction.

7.2.1. Flow in a stenosis

We first compute the steady flow in a rigid stenosis ($\Delta R = -0.4$). In figure 9, we plot the steady spatial evolution of the centerline velocity $u_{x_{|r=0}}$ (fig. 9 left) and of the wall shear stress (WSS) τ_w (fig. 9 right). We use $N_x \in \{800, 1600, 3200\}$ cells and $N_r = 32$ rings. We observe that as we increase the number of cells N_x, the steady multiring numerical solution for the centerline velocity $u_{x_{|r=0}}$ converges towards the steady numerical solution. On the contrary, the steady multiring numerical solution for the WSS τ_w is already converged for $N_x = 800$. Indeed, the number of rings N_r used is sufficient to obtain an accurate description of the shape of the velocity profile near the wall. We also note that the WSS τ_w becomes negative after the stenosis, indicating that the multiring model is able to capture flow recirculations. Finally, the steady WSS τ_w is similar to the one obtained in [42, 58, 56].

In figure 10, we represent the steady velocity profiles taken in $x \in \{0.05, 0.075, 0.1, 0.125, 0.15, 0.175\}\ R_{e,R}R_{|x=0}$. We use $N_x = 3200$ cells and $N_r = 32$ rings. For each recorded position, the steady multiring numerical velocity profiles agree well with the steady numerical velocity profiles. We observe that after the stenosis, a small jet-like region of high velocities forms in the center of the artery and a region of low and negative velocities is created near the wall. These results are coherent with the results presented in figure 9 and with the velocities profiles obtained in [42].

7.2.2. Flow in an aneurysm

We compute here the steady flow in a rigid aneurysm ($\Delta R = +0.4$). In figure 11, we plot the steady spatial evolution of the centerline velocity $u_{x_{|r=0}}$ (fig. 11 left) and of the wall shear stress (WSS) τ_w (fig. 11 right). We use $N_x \in \{800, 1600, 3200\}$ cells and $N_r = 32$ rings. For each quantity, the steady multiring numerical solution converges towards the steady numerical solution. We also note that even though the aneurysm is not large enough to create a flow recirculation, the WSS τ_w is almost negative in the center of the aneurysm. Finally, the steady WSS τ_w is similar to the one obtained in [12, 26].

In figure 12, we represent the steady velocity profiles taken in $x \in \{0.05, 0.075, 0.1, 0.125, 0.15, 0.175\}\ R_{e,R}R_{|x=0}$. We use $N_x = 3200$ cells and $N_r = 32$ rings. For each recorded position, the steady multiring numerical velocity profiles agree well with the steady numerical velocity profiles.

The results presented previously indicate that for a high arterial wall rigidity, the multiring model (23) is able to compute the characteristic steady nonlinear flow features in a rigid artery. Indeed, we have shown that it can describe the nonlinear steady transition from a flat to a Poiseuille velocity profile, the acceleration of

the flow in a stenosis, the deceleration of the flow in a aneurysm as well as small flow recirculations after the stenosis. It can also correctly compute the variation of the WSS and the pressure loss. We are therefore assured that the multiring model (23) correctly describes all relevant steady and unsteady, linear and nonlinear blood flow features in quasi-rigid and elastic straight, constricted (stenosis) and expanded (aneurysm) arteries.

Next, we use the multiring model to compute unsteady blood flow in an elastic stenosis.

8. Unsteady flow in an elastic stenosis

In physiological conditions, the arteries are elastic and the flow of blood is pulsatile in nature. Hence we compute here with the multiring model (23) a periodic flow in an elastic artery. The Womersley number α (eq. (100)), the Reynolds number (eq. $R_{e,R}$ (111)) and the Shapiro number S_h (eq. (38)) are the relevant dimensionless numbers in this example. Here S_h is defined as:

$$S_h = \frac{U_{in}}{c}, \qquad c = \sqrt{\sqrt{\pi}\frac{K}{2\rho}R}. \tag{116}$$

We consider an artery initially at rest (eq. (107)). We impose at the inlet a periodic Pohlhausen velocity profile (eq. (113)), mimicking the flow ejected by the heart in the aorta:

$$u_x\left(x=0,r,t\right) = U_{in}\,\phi_{Polhlausen}\left(r\right)\max\left(0,\,\sin\left(2\pi\frac{t}{T_c}\right)\right), \tag{117}$$

where T_c is the period of the flow. At the outlet we impose a zero reflection coefficient R_t to remove any backward traveling waves. The values of the geometrical and mechanical parameters describing the artery as well as those describing the inlet and outlet boundary conditions are presented in table 6 and are given in "cgs". The final time t_f is large enough to reach a periodic flow regime. The geometrical and mechanical parameters mimic physiological conditions at the root of the aorta, where $R_{e,R} \approx 100$, $\alpha \approx 15$ and $S_h \approx 10^{-2}$. As in the previous section, the stenosis is described by the radius at rest R_0 (eq. (115)) with $x_s = \frac{L}{5}$, $x_f = \frac{3L}{5}$ and $\Delta R = -0.4$.

L	R_0	K	ρ	μ	U_{in}	R_t	T_c	t_f	$R_{e,R}$	α	S_h
$0.25\ R_{e,R}R_{\|x=0}$	1	10^5	1	$\rho\frac{U_{in}R_{\|x=0}}{R_{e,R}}$	S_hc	0	$\frac{2\pi}{\nu}\frac{R_0^2}{\alpha^2}$	$5T_c$	100	15	10^{-2}

Table 6: *Unsteady elastic stenosis example. Geometrical and mechanical parameters describing the artery and the inlet and outlet boundary conditions, all given in "cgs".*

In figure 13, we plot the temporal evolution of the pressure p (fig. 13 top left), of the pressure gradient $\partial_x p$ (fig. 13 top right), of the flow rate Q (fig. 13 bottom left) and of the WSS τ_w (fig. 13 bottom right) in $x \in \{0.025,\, 0.1,\, 0.175\}\, R_{e,R}R_{|x=0}$. We use $N_x = 3200$ cells and $N_r = 32$ rings. We observe that for each recorded positions, a periodic flow regime is reached after 4 periods. During systole $\left(nT_c < t < \frac{3}{2}nT_c,\, n \in \mathbb{N}\right)$, the pulse wave propagates in the artery and the pressure p is higher upstream of the stenosis, in $x = 0.025R_{e,R}R_{|x=0}$. The pressure gradient $\partial_x p$ is therefore negative and the flow rate Q as well as the WSS τ_w are positive. On the contrary, during diastole $\left(\frac{3}{2}nT_c < t < 2nT_c,\, n \in \mathbb{N}\right)$, the pulse wave exits the artery and the pressure p is higher downstream of the stenosis, in $x = 0.175R_{e,R}R_{|x=0}$. The pressure gradient $\partial_x p$ is then positive and the flow rate Q and the WSS τ_w are negative. Moreover, the presence of the stenosis creates a reflection of the incoming pulse wave, resulting in higher pressure values and a smaller flow rate Q upstream the stenosis, in $x = 0.025R_{e,R}R_{|x=0}$. Finally, the WSS is maximum in the stenosis, in $x = 0.1R_{e,R}R_{|x=0}$, as the flow is accelerated due to the constriction.

In figure 14, we decompose the flow motion over one period (the fourth period) and focus on four different instants of the cycle: the end of diastole (or the beginning of systole) at $t = 4T_c$, the peak of systole at $t = 0.25T_c + 4T_c$, the end of systole (or the beginning of diastole) at $t = 0.5T_c + 4T_c$ and the middle of diastole at $t = 0.75T_c + 4T_c$. For each instant, we plot the velocity profiles in the artery (fig. 14 left) and the spatial evolution of the pressure p (fig. 14 center) and the WSS τ_w (fig. 14 right). At times $t = 4T_c$, $t = 0.5T_c + 4T_c$ and $t = 0.75T_c + 4T_c$, we observe that the shapes of the pressure p waveforms are almost identical. The same can be said of the WSS τ_w. At these times, the pressure gradient $\partial_x p$ is positive, indicating that the pulse wave has left the artery. This positive pressure gradient reverses the flow, but only near the wall, as indicated by the negative WSS τ_w. The inertia of the flow in the core of the artery is too strong to observe a complete flow

reversal in one period. At $t = 0.25T_c + 4T_c$, the pressure p and WSS τ_w resemble the steady pressure and WSS observed in figure 9. This indicates that a quasi-steady flow regime is reached at the peak of systole since the period T_c of the flow is larger than the characteristic time of propagation of the pulse wave.

The results presented in figures 13 and 14 are similar to those obtained in [69]. They indicate that the multiring model (23) is capable of describing the unsteady flow in a elastic stenosis and that it computes the expected unsteady flow behaviors such as wave reflections and flow recirculations.

9. Conclusion

We have presented a two-dimensional (2D) nonlinear axisymmetric multiring model to compute blood flow in elastic arteries. This model results from the integration of the RNS-P equations (1) over concentric rings of fluid in an elastic artery, providing a unified framework where both the motion of the fluid and the displacement of the arterial wall are dealt with simultaneously. Its mathematical structure as a system of balance laws allowed us to use a robust, conservative and positive *finite volume* numerical method to compute steady and unsteady linear and nonlinear flows in quasi-rigid and elastic arteries. The multiring model and the numerical method were validated on multiple physiological blood flow examples. For each of the considered test cases, the multiring solution agreed very well with the reference solution for the velocity profiles, the wall shear stress (WSS) and other averaged quantities such as the flow rate or the pressure, even when large arterial wall deformations were considered. In the presence of pathologies such as stenoses or aneurysms, the multiring model captured the expected flow behaviors, and in particular flow recirculation, downstream of the stenosis and in the aneurysm. In comparison, classical one-dimensional (1D) models can only compute average quantities such as the flow rate or the pressure and can not describe flow recirculations. This study shows that the multiring model can serve as a superior alternative to 1D models to accurately compute blood flow in large elastic arteries at a reduced computational cost and could also prove to be a reliable substitute to three-dimensional (3D) models when simple arterial configurations are considered. This method can be extended to other pressure laws to describe the flow in veins and viscoelastic tubes or the propagation of a water hammer (Allevi's equation). In future works, we plan to couple the 2D multiring model with a 1D model and to propose a non-Newtonian 2D multiring model to take into account the effect of aggregation of red blood cells in regions of low shear rate.

Acknowledgments

The authors are grateful to thank J. Sainte-Marie for his helpful remarks and comments.

References

[1] J Alastruey, KH Parker, J Peiró, and SJ Sherwin. Analysing the pattern of pulse waves in arterial networks: a time-domain study. *Journal of Engineering Mathematics*, 64(4):331–351, 2009.

[2] Christopher J Arthurs, Kevin D Lau, Kaleab N Asrress, Simon R Redwood, and C Alberto Figueroa. A mathematical model of coronary blood flow control: simulation of patient-specific three-dimensional hemodynamics during exercise. *American Journal of Physiology-Heart and Circulatory Physiology*, 310(9):H1242–H1258, 2016.

[3] Chloe Audebert, Petru Bucur, Mohamed Bekheit, Eric Vibert, Irene E Vignon-Clementel, and Jean-Frédéric Gerbeau. Kinetic scheme for arterial and venous blood flow, and application to partial hepatectomy modeling. *Computer Methods in Applied Mechanics and Engineering*, 2016.

[4] Emmanuel Audusse, Fayssal Benkhaldoun, Saida Sari, Mohammed Seaid, and Pablo Tassi. A fast finite volume solver for multi-layered shallow water flows with mass exchange. *Journal of Computational Physics*, 272:23–45, 2014.

[5] Emmanuel Audusse and Marie-Odile Bristeau. A well-balanced positivity preserving second-order scheme for shallow water flows on unstructured meshes. *Journal of Computational Physics*, 206(1):311–333, 2005.

[6] Emmanuel Audusse, Marie-Odile Bristeau, Benoît Perthame, and Jacques Sainte-Marie. A multilayer Saint-Venant system with mass exchanges for shallow water flows. derivation and numerical validation. *ESAIM: Mathematical Modelling and Numerical Analysis*, 45(01):169–200, 2011.

[7] Gabriel R Barrenechea and Franz Chouly. A finite element method for the resolution of the reduced navier-stokes/prandtl equations. *ZAMM-Journal of Applied Mathematics and Mechanics/Zeitschrift für Angewandte Mathematik und Mechanik*, 89(1):54–68, 2009.

[8] Alfredo Bermúdez and Ma Elena Vázquez. Upwind methods for hyperbolic conservation laws with source terms. *Computers & Fluids*, 23(8):1049–1071, 1994.

[9] David Bessems, Marcel Rutten, and Frans Van De Vosse. A wave propagation model of blood flow in large vessels using an approximate velocity profile function. *Journal of Fluid Mechanics*, 580:145–168, 2007.

[10] François Bouchut. Construction of BGK models with a family of kinetic entropies for a given system of conservation laws. *Journal of Statistical Physics*, 95(1-2):113–170, 1999.

[11] Marie-Odile Bristeau and Benoit Coussin. Boundary conditions for the shallow water equations solved by kinetic schemes. 2001.

[12] R Budwig, D Elger, H Hooper, and J Slippy. Steady flow in abdominal aortic aneurysm models. *Journal of biomechanical engineering*, 115(4A):418–423, 1993.

[13] Sunčica Čanić, Craig J Hartley, Doreen Rosenstrauch, Josip Tambača, Giovanna Guidoboni, and Andro Mikelić. Blood flow in compliant arteries: an effective viscoelastic reduced model, numerics, and experimental validation. *Annals of Biomedical Engineering*, 34(4):575–592, 2006.

[14] Sunčica Čanić, Daniele Lamponi, Andro Mikelic, and Josip Tambača. Self-consistent effective equations modeling blood flow in medium-to-large compliant arteries. *Multiscale Modeling & Simulation*, 3(3):559–596, 2005.

[15] Vincenzo Casulli, Michael Dumbser, and Eleuterio F Toro. Semi-implicit numerical modeling of axially symmetric flows in compliant arterial systems. *International journal for numerical methods in biomedical engineering*, 28(2):257–272, 2012.

[16] Franz Chouly and P-Y Lagrée. Comparison of computations of asymptotic flow models in a constricted channel. *Applied Mathematical Modelling*, 36(12):6061–6071, 2012.

[17] Richard Courant, Kurt Friedrichs, and Hans Lewy. On the partial difference equations of mathematical physics. *IBM journal*, 11(2):215–234, 1967.

[18] Olivier Delestre, Arthur R Ghigo, J-M Fullana, and P-Y Lagrée. A shallow water with variable pressure model for blood flow simulation. *Networks and Heterogeneous Media*, 11(1):69–87, 2016.

[19] Olivier Delestre and P-Y Lagrée. A well-balanced finite volume scheme for blood flow simulation. *International Journal for Numerical Methods in Fluids*, 72(2):177–205, 2012.

[20] P Di Achille, G Tellides, CA Figueroa, and JD Humphrey. A haemodynamic predictor of intraluminal thrombus formation in abdominal aortic aneurysms. In *Proc. R. Soc. A*, volume 470, page 20140163. The Royal Society, 2014.

[21] Michael Dumbser, Uwe Iben, and Matteo Ioriatti. An efficient semi-implicit finite volume method for axially symmetric compressible flows in compliant tubes. *Applied Numerical Mathematics*, 89:24–44, 2015.

[22] Leonhard Euler. Principia pro motu sanguinis per arterias determinando. *Opera posthuma mathematica et physica anno*, pages 814–823, 1844.

[23] Charbel Farhat, Philippe Geuzaine, and Céline Grandmont. The discrete geometric conservation law and the nonlinear stability of ale schemes for the solution of flow problems on moving grids. *Journal of Computational Physics*, 174(2):669–694, 2001.

[24] Enrique Domingo Fernández-Nieto, EH Koné, T Morales De Luna, and R Bürger. A multilayer shallow water system for polydisperse sedimentation. *Journal of Computational Physics*, 238:281–314, 2013.

[25] C Alberto Figueroa, Irene E Vignon-Clementel, Kenneth E Jansen, Thomas JR Hughes, and Charles A Taylor. A coupled momentum method for modeling blood flow in three-dimensional deformable arteries. *Computer methods in applied mechanics and engineering*, 195(41):5685–5706, 2006.

[26] Ender A Finol and Cristina H Amon. Flow-induced wall shear stress in abdominal aortic aneurysms: Part i-steady flow hemodynamics. *Computer Methods in Biomechanics & Biomedical Engineering*, 5(4):309–318, 2002.

[27] Joaquín Flores, Jordi Alastruey, and Eugenia Corvera Poiré. A novel analytical approach to pulsatile blood flow in the arterial network. *Annals of biomedical engineering*, pages 1–22, 2016.

[28] Luca Formaggia, Daniele Lamponi, and Alfio Quarteroni. One-dimensional models for blood flow in arteries. *Journal of engineering mathematics*, 47(3-4):251–276, 2003.

[29] Yuan-cheng Fung. *Biomechanics: circulation*. Springer Science & Business Media, 2013.

[30] Laurent Gosse and Alain-Yves LeRoux. Un schéma-équilibre adapté aux lois de conservation scalaires non-homogènes. *CR Acad. Sci. Paris Sér. I Math*, 323(5):543–546, 1996.

[31] Joshua M Greenberg and Alain-Yves LeRoux. A well-balanced scheme for the numerical processing of source terms in hyperbolic equations. *SIAM Journal on Numerical Analysis*, 33(1):1–16, 1996.

[32] Gerhard A Holzapfel, Thomas C Gasser, and Ray W Ogden. A new constitutive framework for arterial wall mechanics and a comparative study of material models. *Journal of elasticity and the physical science of solids*, 61(1-3):1–48, 2000.

[33] Thomas JR Hughes, Wing Kam Liu, and Thomas K Zimmermann. Lagrangian-eulerian finite element formulation for incompressible viscous flows. *Computer methods in applied mechanics and engineering*, 29(3):329–349, 1981.

[34] HJ Kim, IE Vignon-Clementel, JS Coogan, CA Figueroa, KE Jansen, and CA Taylor. Patient-specific modeling of blood flow and pressure in human coronary arteries. *Annals of biomedical engineering*, 38(10):3195–3209, 2010.

[35] DJ Korteweg. Über die fortpflanzungsgeschwindigkeit des schalles in elastischen röhren. *Annalen der Physik*, 241(12):525–542, 1878.

[36] P-Y Lagrée. An inverse technique to deduce the elasticity of a large artery. *The European Physical Journal Applied Physics*, 9(02):153–163, 2000.

[37] Pierre-Yves Lagrée and Sylvie Lorthois. The rns/prandtl equations and their link with other asymptotic descriptions: application to the wall shear stress scaling in a constricted pipe. *International Journal of Engineering Science*, 43(3):352–378, 2005.

[38] John W Lambert. On the nonlinearities of fluid flow in nonrigid tubes. *Journal of the Franklin Institute*, 266(2):83–102, 1958.

[39] SC Ling and HB Atabek. A nonlinear analysis of pulsatile flow in arteries. *Journal of Fluid Mechanics*, 55(03):493–511, 1972.

[40] Matthias Mayr, Thomas KloİĹppel, Wolfgang A Wall, and Michael W Gee. A temporal consistent monolithic approach to fluid-structure interaction enabling single field predictors. *SIAM Journal on Scientific Computing*, 37(1):B30–B59, 2015.

[41] A Isebree Moens. *Die pulskurve*. EJ Brill, 1878.

[42] Brian Edson Morgan and Donald F Young. An integral method for the analysis of flow in arterial stenoses. *Bulletin of Mathematical Biology*, 36:39–53, 1974.

[43] Lucas O Müller, Carlos Parés, and Eleuterio F Toro. Well-balanced high-order numerical schemes for one-dimensional blood flow in vessels with varying mechanical properties. *Journal of Computational Physics*, 242:53–85, 2013.

[44] Lucas O Müller and Eleuterio F Toro. A global multiscale mathematical model for the human circulation with emphasis on the venous system. *International journal for numerical methods in biomedical engineering*, 30(7):681–725, 2014.

[45] Karl Perktold. On the paths of fluid particles in an axisymmetrical aneurysm. *Journal of biomechanics*, 20(3):311–317, 1987.

[46] Karl Pohlhausen. Zur näherungsweisen integration der differentialgleichung der iaminaren grenzschicht. *ZAMM-Journal of Applied Mathematics and Mechanics/Zeitschrift für Angewandte Mathematik und Mechanik*, 1(4):252–290, 1921.

[47] María Teresa Politi, Arthur Ghigo, Juan Manuel Fernández, Ismaïl Khelifa, Julien Gaudric, José María Fullana, and Pierre-Yves Lagrée. The dicrotic notch analyzed by a numerical model. *Computers in biology and medicine*, 72:54–64, 2016.

[48] Alfio Quarteroni, Alessandro Veneziani, and Christian Vergara. Geometric multiscale modeling of the cardiovascular system, between theory and practice. *Computer Methods in Applied Mechanics and Engineering*, 302:193–252, 2016.

[49] Abhay B Ramachandra, Andrew M Kahn, and Alison L Marsden. Patient-specific simulations reveal significant differences in mechanical stimuli in venous and arterial coronary grafts. *Journal of Cardiovascular Translational Research*, 9(4):279–290, 2016.

[50] PL Roe. Upwind differencing schemes for hyperbolic conservation laws with source terms. In *Nonlinear hyperbolic problems*, pages 41–51. Springer, 1987.

[51] Masashi Saito, Yuki Ikenaga, Mami Matsukawa, Yoshiaki Watanabe, Takaaki Asada, and Pierre-Yves Lagrée. One-dimensional model for propagation of a pressure wave in a model of the human arterial network: comparison of theoretical and experimental results. *Journal of Biomechanical Engineering*, 133(12):121005, 2011.

[52] Sethuraman Sankaran, Mahdi Esmaily Moghadam, Andrew M Kahn, Elaine E Tseng, Julius M Guccione, and Alison L Marsden. Patient-specific multiscale modeling of blood flow for coronary artery bypass graft surgery. *Annals of biomedical engineering*, 40(10):2228–2242, 2012.

[53] Hermann Schlichting. *Boundary-layer theory*. McGraw-Hill, 1968.

[54] Ascher H Shapiro. Steady flow in collapsible tubes. *Journal of Biomechanical Engineering*, 99(3):126–147, 1977.

[55] SJ Sherwin, L Formaggia, J Peiro, and V Franke. Computational modelling of 1D blood flow with variable mechanical properties and its application to the simulation of wave propagation in the human arterial system. *International Journal for Numerical Methods in Fluids*, 43(6-7):673–700, 2003.

[56] John M Siegel, Christos P Markou, David N Ku, and SR Hanson. A scaling law for wall shear rate through an arterial stenosis. *Journal of biomechanical engineering*, 116(4):446–451, 1994.

[57] A Siviglia and M Toffolon. Steady analysis of transcritical flows in collapsible tubes with discontinuous mechanical properties: implications for arteries and veins. *Journal of Fluid Mechanics*, 736:195–215, 2013.

[58] FT Smith. Flow through constricted or dilated pipes and channels: Part 2. *The Quarterly Journal of Mechanics and Applied Mathematics*, 29(3):365–376, 1976.

[59] Charles A Taylor, Thomas JR Hughes, and Christopher K Zarins. Finite element modeling of blood flow in arteries. *Computer methods in applied mechanics and engineering*, 158(1):155–196, 1998.

[60] Tayfun E Tezduyar. Computation of moving boundaries and interfaces and stabilization parameters. *International Journal for Numerical Methods in Fluids*, 43(5):555–575, 2003.

[61] Tayfun E Tezduyar, Sunil Sathe, Timothy Cragin, Bryan Nanna, Brian S Conklin, Jason Pausewang, and Matthew Schwaab. Modelling of fluid–structure interactions with the space–time finite elements: Arterial fluid mechanics. *International Journal for Numerical Methods in Fluids*, 54(6-8):901–922, 2007.

[62] Llewellyn Hilleth Thomas. Elliptic problems in linear difference equations over a network. *Watson Sci. Comput. Lab. Rept., Columbia University, New York*, 1, 1949.

[63] Irene E Vignon-Clementel, Alison L Marsden, and Jeffrey A Feinstein. A primer on computational simulation in congenital heart disease for the clinician. *Progress in Pediatric Cardiology*, 30(1):3–13, 2010.

[64] Lei Wang, Baochang Shi, and Zhenhua Chai. A lattice boltzmann study of the asymmetry effect on the hemodynamics in stented fusiform aneurysms. *Computers & Mathematics with Applications*, 71(1):328–348, 2016.

[65] Xiaofei Wang, Jose-Maria Fullana, and Pierre-Yves Lagrée. Verification and comparison of four numerical schemes for a 1D viscoelastic blood flow model. *Computer methods in biomechanics and biomedical engineering*, 18(15):1704–1725, 2015.

[66] Sven Øivind Wille. Pulsatile pressure and flow in an arterial aneurysm simulated in a mathematical model. *Journal of biomedical engineering*, 3(2):153–158, 1981.

[67] Sven Øivind Wille and Lars Walløe. Pulsatile pressure and flow in arterial stenoses simulated in a mathematical model. *Journal of biomedical engineering*, 3(1):17–24, 1981.

[68] J R Womersley. XXIV. Oscillatory motion of a viscous liquid in a thin-walled elastic tube—I: The linear approximation for long waves. *The London, Edinburgh, and Dublin Philosophical Magazine and Journal of Science*, 46(373):199–221, 1955.

[69] Donald F Young, Neal R Cholvin, and Allan C Roth. Pressure drop across artificially induced stenoses in the femoral arteries of dogs. *Circulation research*, 36(6):735–743, 1975.

[70] Akbar Zaman, Nasir Ali, and O Anwar Bég. Numerical simulation of unsteady micropolar hemodynamics in a tapered catheterized artery with a combination of stenosis and aneurysm. *Medical & biological engineering & computing*, pages 1–14, 2015.

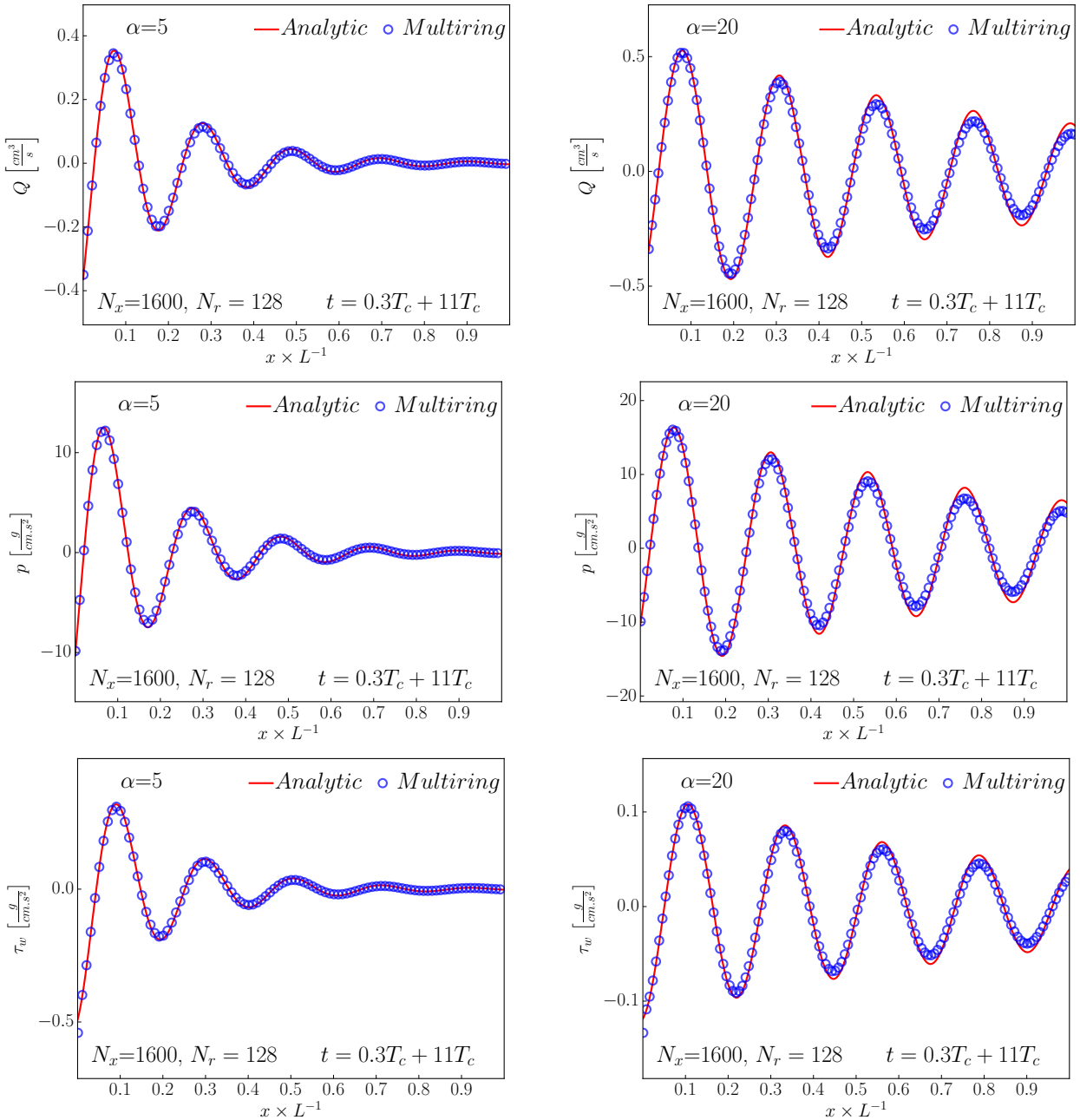

Figure 3: *Elastic Womersley example. Comparison between the flow rate Q, the pressure p and the WSS τ_w obtained with the analytic Womersley solution (—) and with the multiring model (○) using $N_x = 1600$ cells and $N_r = 128$ rings, at time $t = 0.3T_c + 11T_c$ for $\alpha = 5$ (left) and $\alpha = 20$ (right). We observe that the multiring solutions agree well with the analytic solutions.*

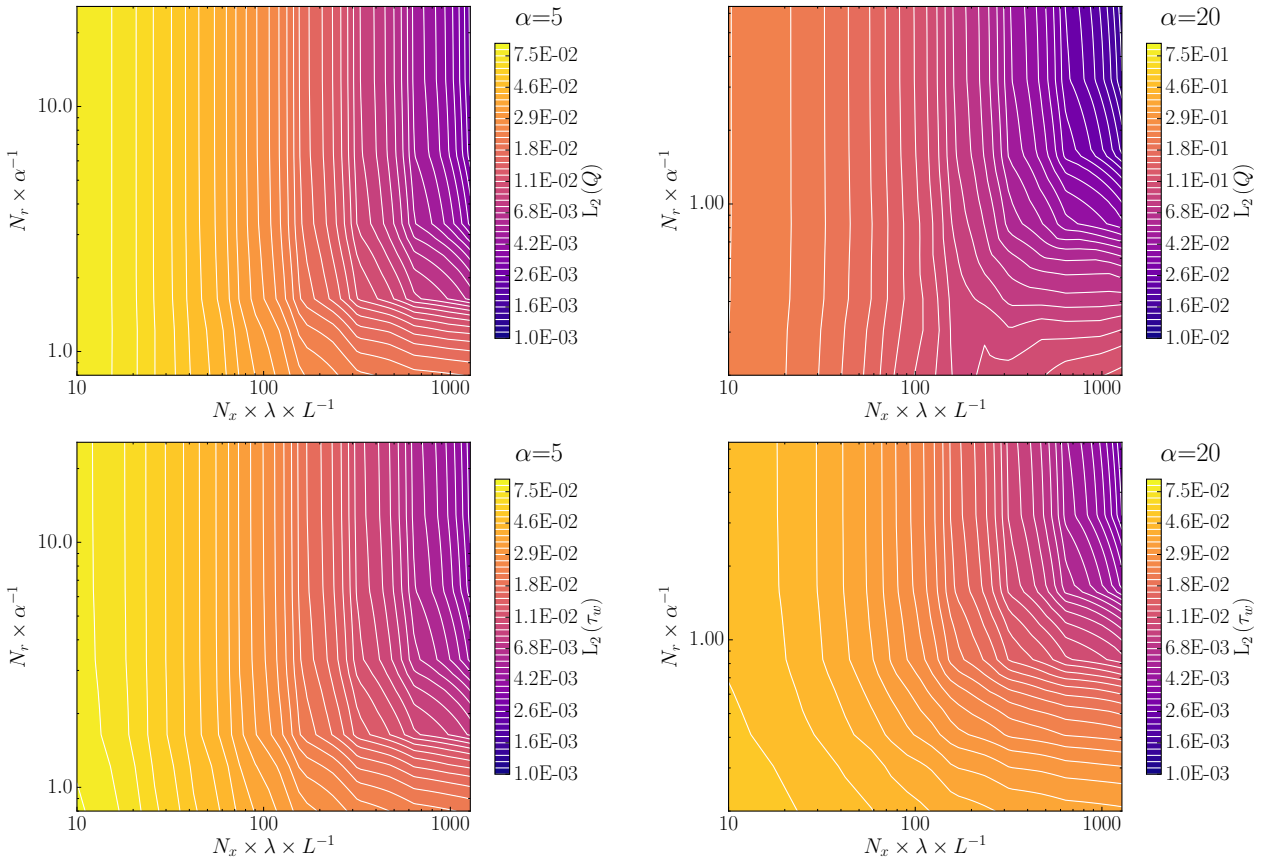

Figure 4: *Elastic Womersley example. Phase diagram of the L_2 spatial error between the Womersley and the multiring solutions as a function of $\lambda N_x/L$ and of N_r/α for $\alpha = 5$ (left) and $\alpha = 20$ (right) at time $t = 0.3T_c + 11T_c$. For low values of $\lambda N_x/L$, increasing N_r/α does not decrease the error significantly, whereas increasing $\lambda N_x/L$ does. On the contrary, for high values of $\lambda N_x/L$, increasing N_r/α significantly decreases the error, whereas increasing $\lambda N_x/L$ does not.*

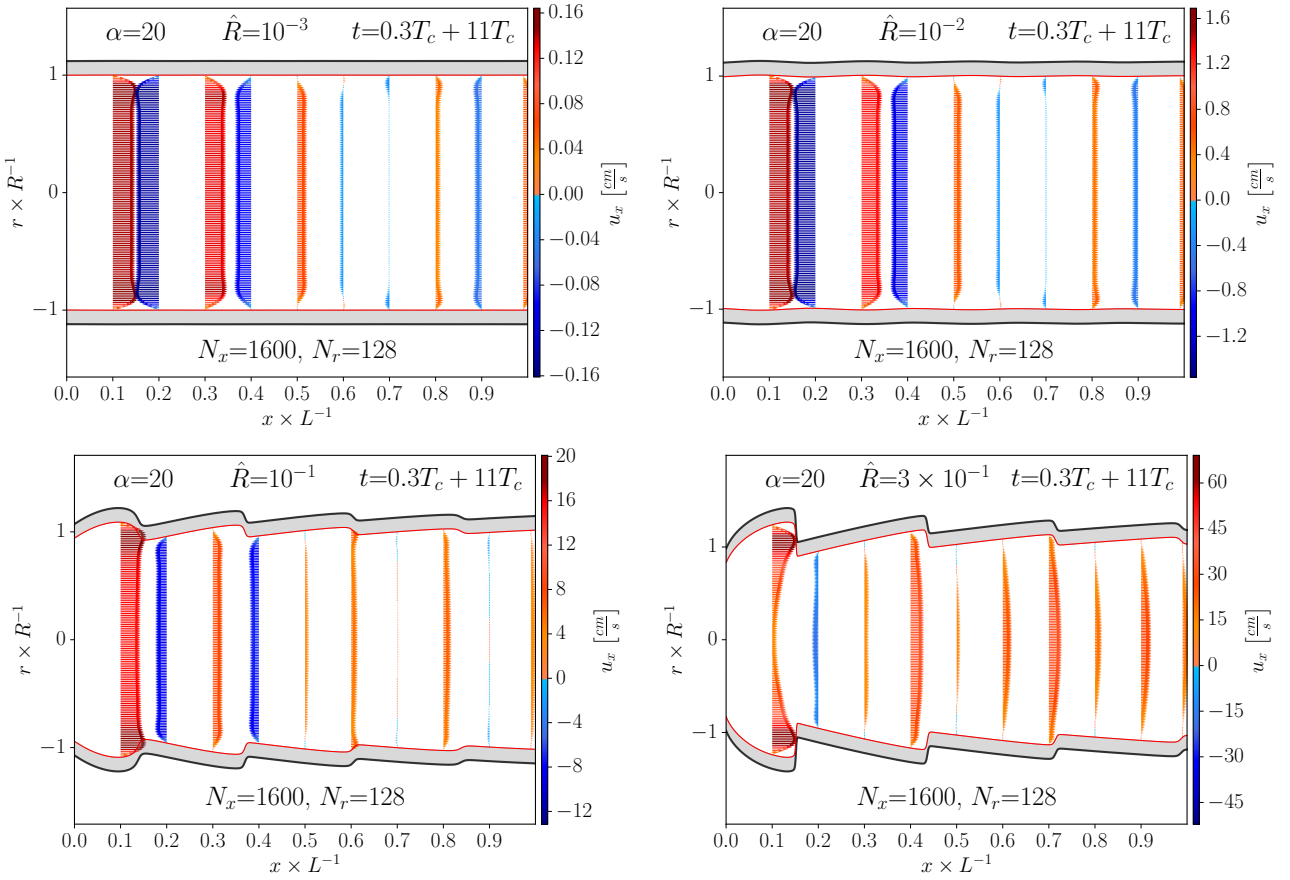

Figure 5: *Elastic Womersley example. Snapshots of the spatial evolution of the axial velocity u_x at $t = 0.3T_c + 11T_c$ obtained using $N_x = 1600$ cells and $N_r = 128$ rings for $\alpha = 20$ and $\hat{R} \in \{10^{-3}, 10^{-2}, 10^{-1}, 3 \times 10^{-1}\}$. We observe that the multiring model is able to compute linear and nonlinear flow behaviors with small and large wall deformations.*

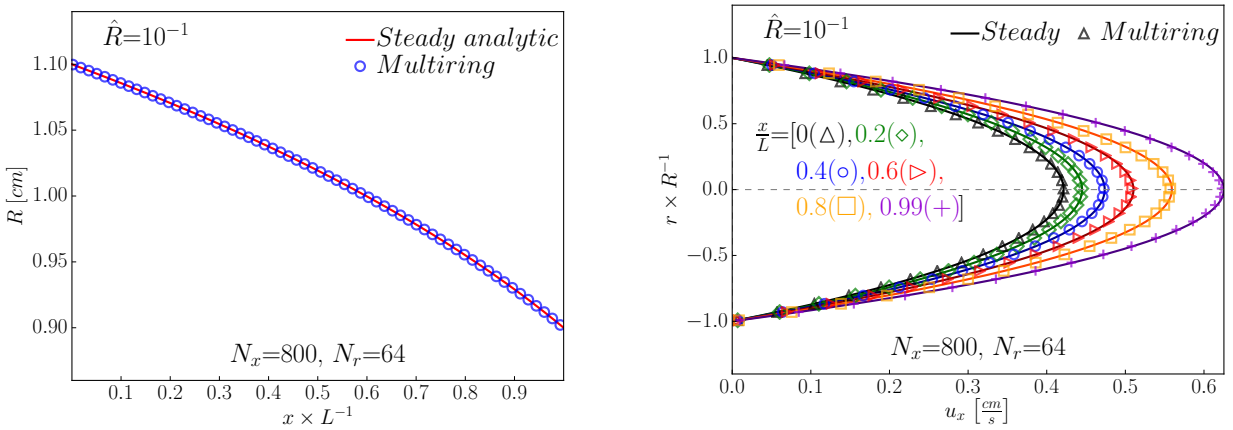

Figure 6: *Steady linear elastic Poiseuille example. Comparison between the steady radius R (left) and the steady axial velocity profiles u_x (right) taken in $x \in \{0\,(\Delta)\,,\ 0.2\,(\diamond)\,,\ 0.4\,(\circ)\,,\ 0.6\,(\triangleright)\,,\ 0.8\,(\square)\,,\ 0.99\,(+)\}\,L$ obtained with the analytic Poiseuille solution (—) and with the multiring model (marks) using $N_x = 800$ cells and $N_r = 64$ rings. We observe a good agreement between the analytic and the multiring numerical solutions.*

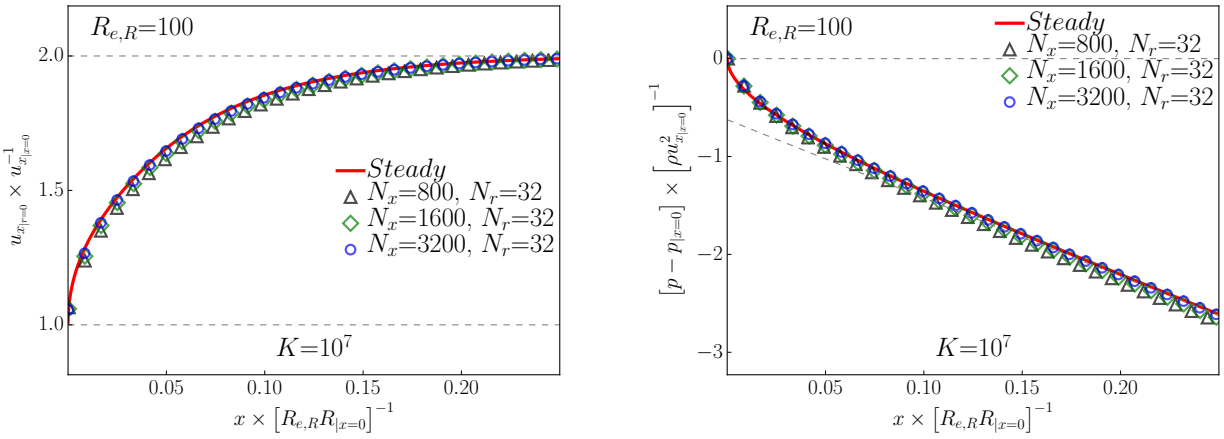

Figure 7: *Steady rigid Poiseuille example. Comparison between the steady centerline velocity $u_{x_{|r=0}}$ (left) and the steady pressure p (right) obtained with the steady code [37] (—) and with the multiring model using $N_x \in \{800\,(\Delta)\,, 1600\,(\diamond)\,, 3200\,(\circ)\}$ cells and $N_r = 32$ rings. On the left plot, the dashed lines represent the value of the flat centerline velocity ($u_{x_{|r=0}} = u_{x_{|x=0}}$) and the Poiseuille centerline velocity ($u_{x_{|r=0}} = 2u_{x_{|x=0}}$). On the right plot, the dashed line represents the pressure drop $-8x/\left(R_{e,R}R_{|x=0}\right)$ of a Poiseuille flow. For each quantity, the steady multiring numerical solution converges towards the steady numerical solution and we observe the transition from a flat to a Poiseuille velocity profile.*

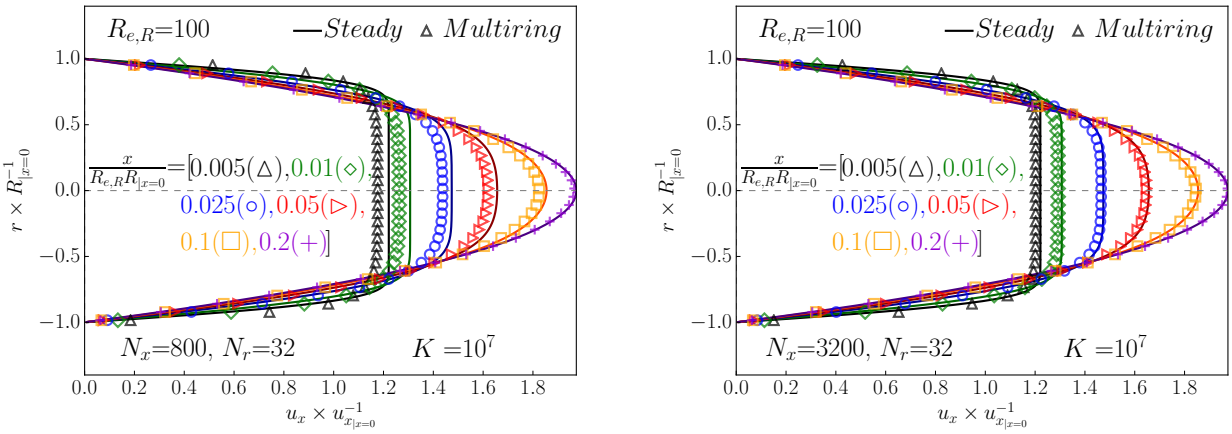

Figure 8: *Steady rigid Poiseuille example. Comparison between the steady velocity profiles obtained with the steady code [37] (—) and with the multiring model using $N_x \in \{800$ (left), 3200 (right)$\}$ cells and $N_r = 32$ rings, taken in $x \in \{0.005\,(\Delta)\,, 0.01\,(\diamond)\,, 0.025\,(\circ)\,, 0.05\,(\triangleright)\,, 0.1\,(\square)\,, 0.2\,(+)\}\, R_{e,R}R_{|x=0}$. We observe that the steady multiring velocity profiles converge towards the steady velocity profiles and accurately reproduce the transition from the Blasius to the Poiseuille flow regime.*

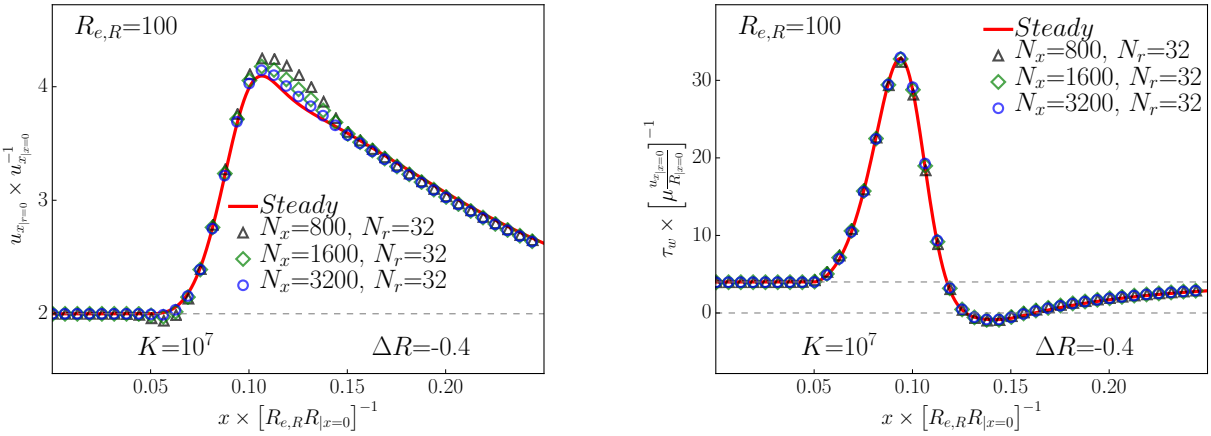

Figure 9: *Steady rigid stenosis example. Comparison between the steady centerline velocity $u_{x_{|r=0}}$ (left) and the steady WSS τ_w (right) obtained with the steady code [37] (—) and with the multiring model using $N_x \in \{800\,(\Delta)\,,\ 1600\,(\diamond)\,,\ 3200\,(\circ)\}$ cells and $N_r = 32$ rings. On the left plot, the dashed line represents the value of the Poiseuille centerline velocity ($u_{x_{|r=0}} = 2u_{x_{|x=0}}$). On the right plot, the dashed line represents the value of the Poiseuille WSS ($\tau_w = 4\mu u_{x_{|x=0}}/R_{|x=0}$). For each quantity, the steady multiring numerical solution converges towards the steady numerical solution.*

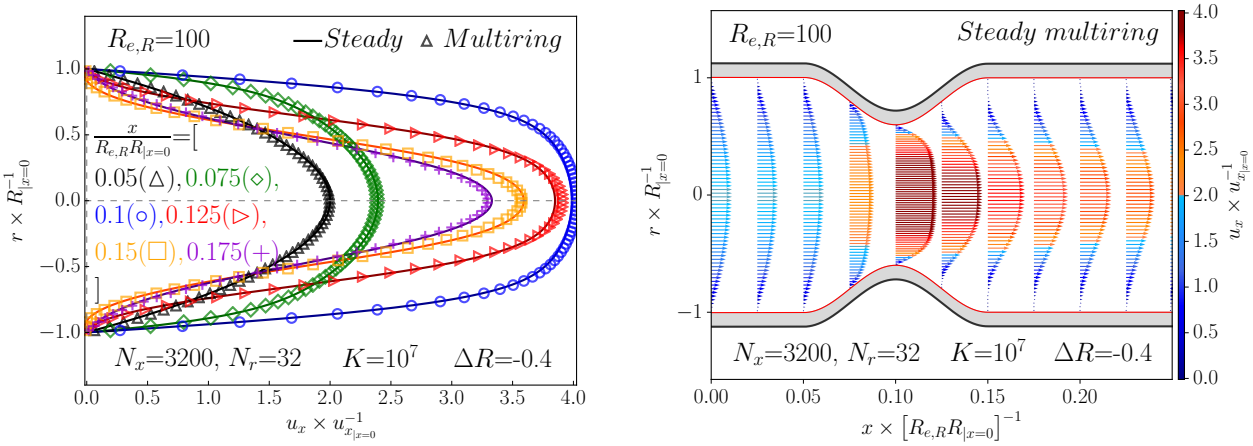

Figure 10: *Steady rigid stenosis example. Comparison between the steady velocity profiles obtained with the steady code [37] (—) and with the multiring model using $N_x = 3200$ cells and $N_r = 32$ rings, taken in $x \in \{0.05\,(\Delta)\,,\ 0.075\,(\diamond)\,,\ 0.1\,(\circ)\,,\ 0.125\,(\triangleright)\,,\ 0.15\,(\square)\,,\ 0.175\,(+)\}\, R_{e,R} R_{|x=0}$. We observe that the multiring velocity profiles are in good accord with the steady velocity profiles.*

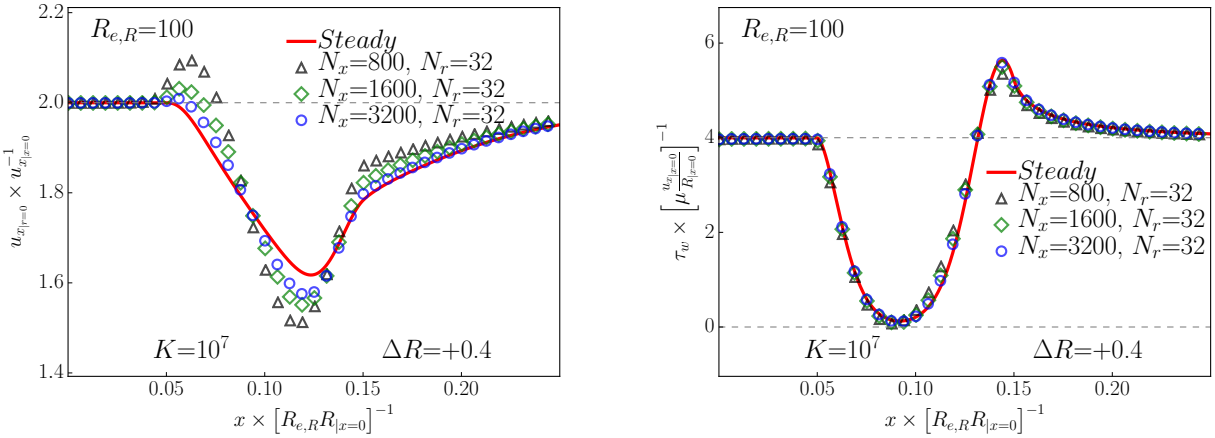

Figure 11: *Steady rigid aneurysm example. Comparison between the steady centerline velocity $u_{x_{|r=0}}$ (left) and the steady WSS τ_w (right) obtained with the steady code [37] (—) and with the multiring model using $N_x \in \{800\,(\Delta)\,,\ 1600\,(\diamond)\,,\ 3200\,(\circ)\}$ cells and $N_r = 32$ rings. On the left plot, the dashed line represents the value of the Poiseuille centerline velocity ($u_{x_{|r=0}} = 2u_{x_{|x=0}}$). On the right plot, the dashed line represents the value of the Poiseuille WSS ($\tau_w = 4\mu u_{x_{|x=0}}/R_{|x=0}$). For each quantity, the steady multiring numerical solution converges towards the steady numerical solution.*

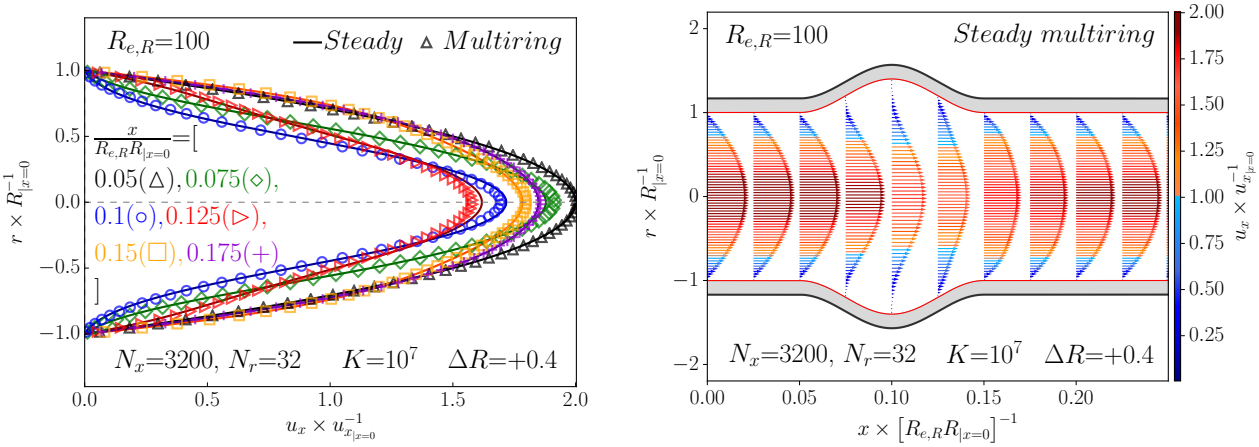

Figure 12: *Steady rigid aneurysm example. Comparison between the steady velocity profiles obtained with the steady code [37] (—) and with the multiring model using $N_x = 3200$ cells and $N_r = 32$ rings, taken in $x \in \{0.05\,(\Delta)\,,\ 0.075\,(\diamond)\,,\ 0.1\,(\circ)\,,\ 0.125\,(\triangleright)\,,\ 0.15\,(\square)\,,\ 0.175\,(+)\}\,R_{e,R}R_{|x=0}$. We observe that the steady multiring velocity profiles are in good accord with the steady velocity profiles.*

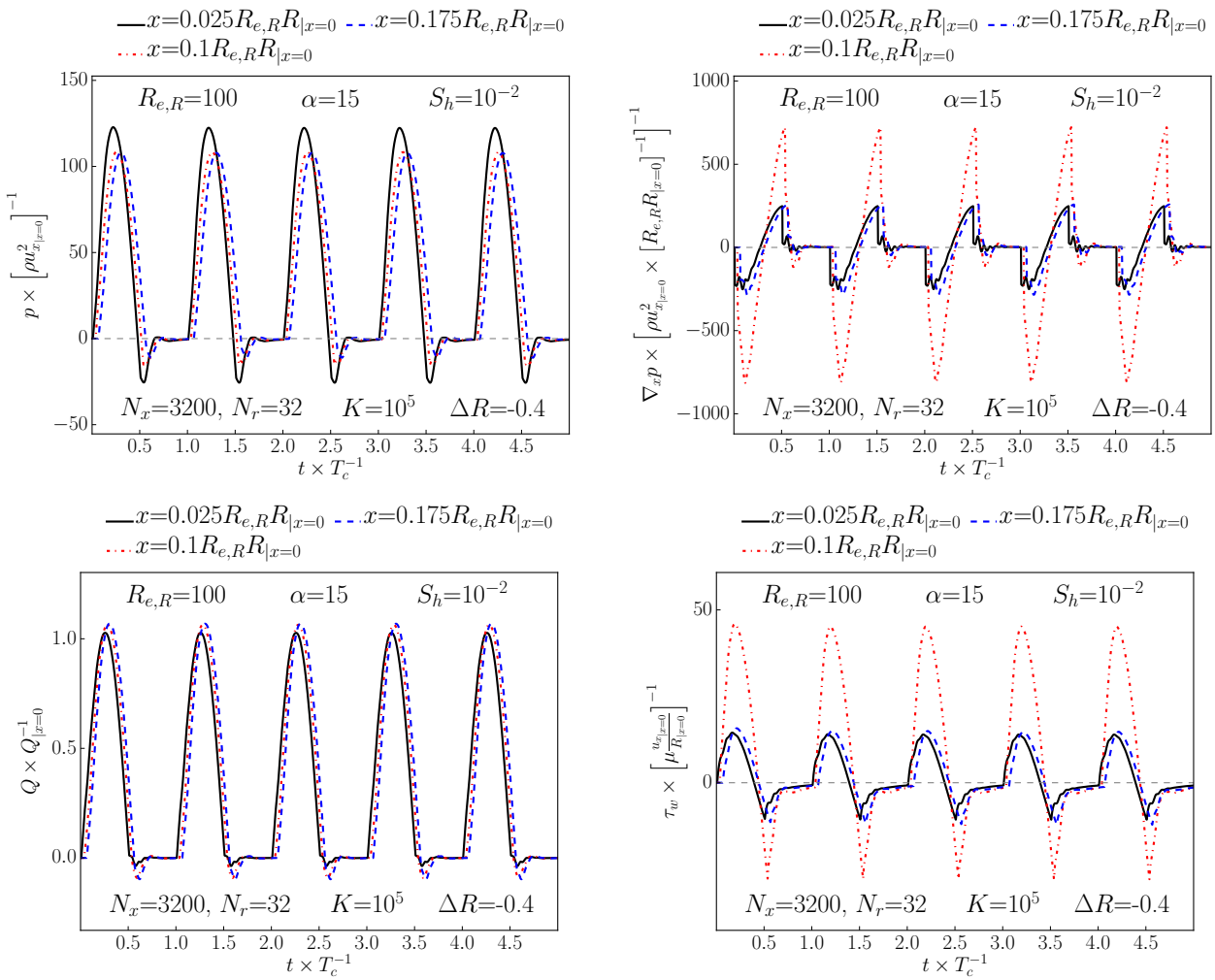

Figure 13: *Unsteady elastic stenosis example. Temporal evolution of the pressure p (top left), the pressure gradient $\partial_x p$ (top right), the flow rate Q (bottom left) and the WSS τ_w (bottom right) in $x \in \{0.025\,(\text{—}),\, 0.1\,(--),\, 0.175\,(-\cdot)\}\, R_{e,R}R_{|x=0}$ obtained using $N_x = 3200$ cells and $N_r = 32$ rings. We observe that after four cycles a periodic state is reached. We notice evidence of wave propagation and reflection as well as flow recirculation.*

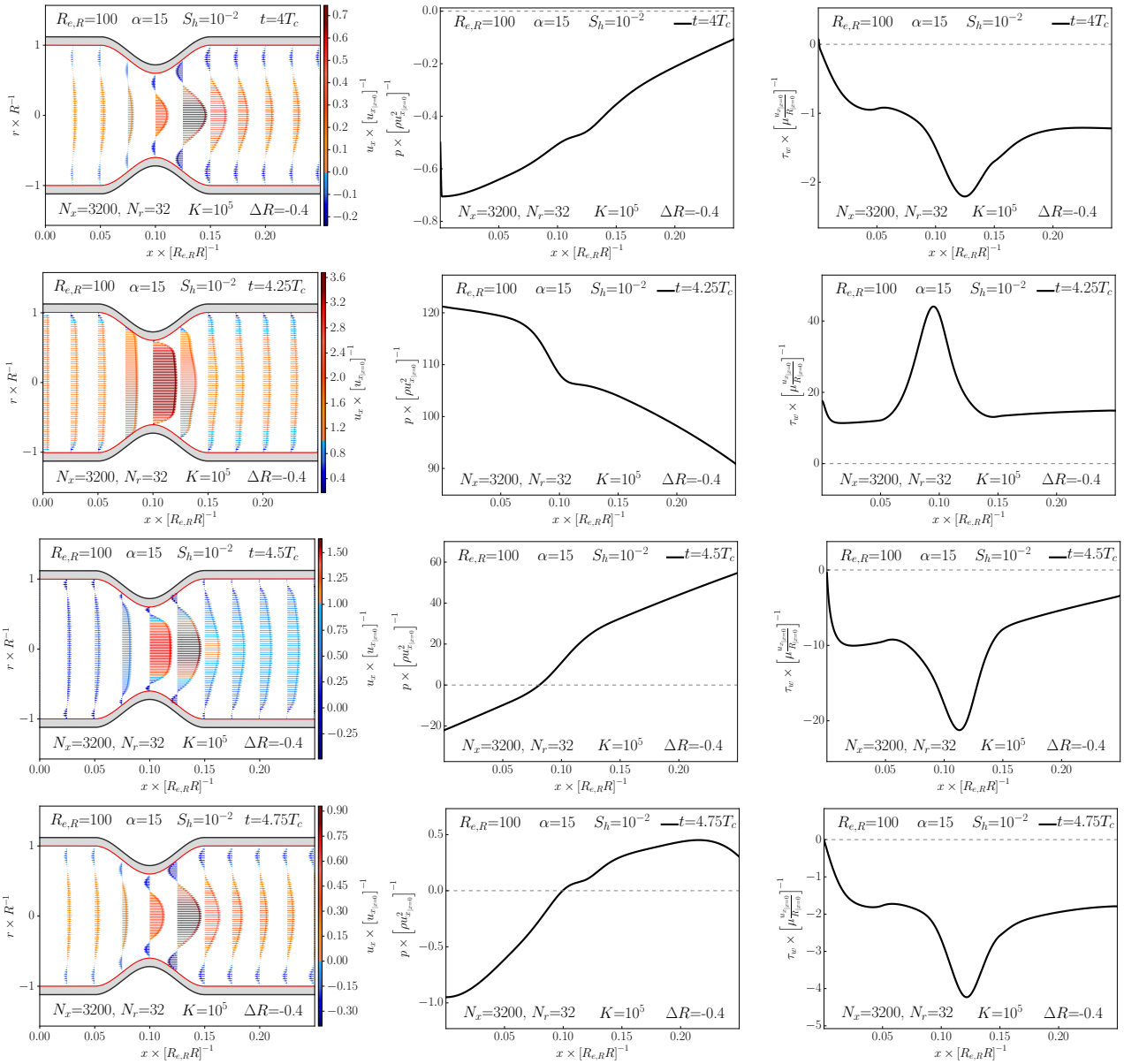

Figure 14: *Unsteady elastic stenosis example. Snapshots of the spatial evolution of the axial velocity u_x (left), the pressure p (center) and the WSS τ_w (right) at $t \in \{0, 0.25, 0.5, 0.75\}\, T_c + 4T_c$ obtained using $N_x = 3200$ cells and $N_r = 32$ rings. We observe a backflow near the wall created by the positive pressure gradient at $t \in \{0, 0.5, 0.75\}\, T_c + 4T_c$. However, the inertia in the core of the artery is too strong to observe a complete flow reversal in one period. At the peak of systole $t = 0.25T_c + 4T_c$, the shapes of the pressure p and the WSS τ_w resemble those obtained in figure 9, indicating that a quasi-steady flow regime is reached.*